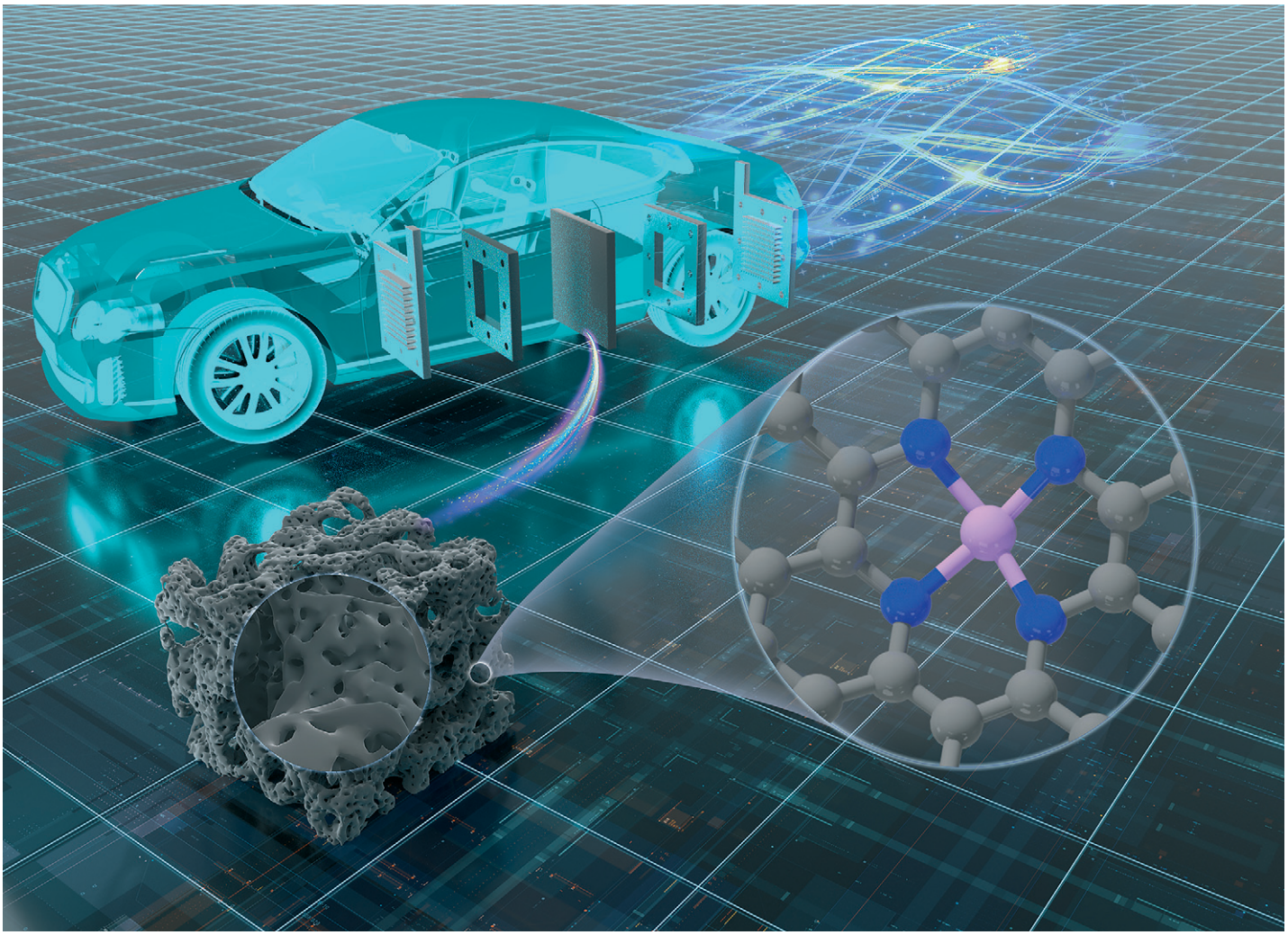

Showcasing research from Wei Xing's laboratory, Changchun Institute of Applied Chemistry, Chinese Academy of Sciences, Changchun, China.

Non-noble metals as activity sites for ORR catalysts in proton exchange membrane fuel cells (PEMFCs)

Proton exchange membrane fuel cells (PEMFCs) have great potential to become the next generation green energy technique, but its application is limited by the slow kinetics of the cathode oxygen reduction reaction (ORR) in acidic medium.

As featured in:

See Xian Wang, Junjie Ge, Wei Xing *et al.*, *Ind. Chem. Mater.*, 2023, **1**, 388.

ROYAL SOCIETY OF CHEMISTRY

Industrial Chemistry & Materials

Industrial Chemistry & Materials

ROYAL SOCIETY OF CHEMISTRY

REVIEW

View Article Online
View Journal | View Issue

Check for updates

Cite this: *Ind. Chem. Mater.*, 2023, **1**, 388

Non-noble metals as activity sites for ORR catalysts in proton exchange membrane fuel cells (PEMFCs)

Jinjing Tao,[ab] Xian Wang,*[ab] Mingjun Xu,[ab] Changpeng Liu,[ab] Junjie Ge *[ab] and Wei Xing *[ab]

Proton exchange membrane fuel cells (PEMFCs) have great potential to become the next generation green energy technique, but their application is limited by the slow kinetics of the cathode oxygen reduction reaction (ORR) in acidic medium. Meanwhile, the high price of Pt-based catalysts, which are now widely used commercially, has raised the cost of PEMFCs. Therefore, non-noble metal ORR catalysts as alternatives to Pt-based group metals (PGM) have attracted much attention. However, there is still a big gap between the performance of non-noble metal catalysts and commercial Pt/C catalysts in acidic environment. Recently, it has been realized that the performance of catalysts is closely related to the structure of catalytically active sites. Inspired by this, in this review, we firstly introduced the development and breakthrough of non-noble metals as activity sites. We then briefly summarized their catalytic mechanisms, and put forward some suggestions on how to improve the activity and stability of non-noble metal ORR catalysts.

Received 5th January 2023,
Accepted 8th March 2023

DOI: 10.1039/d3im00002h

rsc.li/icm

Keywords: ORR; Non-noble metal single atom catalysts; Active site; Fuel cell.

1 Introduction

Proton exchange membrane fuel cells (PEMFCs) can easily convert hydrogen energy to electricity without igniting, which has been widely studied because of its advantages of high energy conversion efficiency, no pollution, low noise and strong endurance.[1] PEMFCs consist of two half reactions, *i.e.*, the oxygen reduction reaction (ORR) and hydrogen oxidation reaction (HOR), respectively. The kinetics of the ORR at the cathode is much slower than that of the HOR at the anode. Therefore, it is essential to improve the ORR kinetics for promoting fuel cell performance.[2] Commercial Pt-based catalysts are widely used in the cathodic ORR, however, their high price and low abundance lead to high catalyst cost and

[a] *State Key Laboratory of Electroanalytical Chemistry, Jilin Province Key Laboratory of Low Carbon Chemistry Power, Changchun Institute of Applied Chemistry, Chinese Academy of Sciences, Changchun, 130022, China. E-mail: xwang@ciac.ac.cn, xingwei@ciac.ac.cn*

[b] *School of Applied Chemistry and Engineering, University of Science and Technology of China, Hefei, 230026, China. E-mail: gejunjie@ustc.edu.cn*

Jinjing Tao

Jinjing Tao received her BS from Wuhan University of Technology in 2021. She is currently a master student in Physical Chemistry under the supervision of Prof. Wei Xing at the Changchun Institute of Applied Chemistry, Chinese Academy of Sciences, China. Now her research interests lie in the design and preparation of cathode oxygen reduction reaction catalysts for PEMFCs.

Xian Wang

Dr. Xian Wang received his Ph.D. in physical chemistry from the University of Science and Technology of China in 2021. Then, he worked at Changchun Institute of Applied Chemistry as an assistant researcher. His research interests cover fuel cells and anti-poisoning catalysts.

thereby limit the commercialization of PEMFCs. In order to meet the application requirements of PEMFCs, ORR catalysts that are highly efficient, stable, and low-cost (PGM-free) for use in acidic environments are urgently needed.[3]

Macrocyclic-derived catalysts, as an alternative to Pt based catalysts, have been studied intensively since 1964, when Jasinski initially found phthalocyanine cobalt as a kind of macrocyclic compound showing promising activity toward the ORR.[4] In the past few decades, non-noble metal-based catalysts have made tremendous progress towards the ORR. However, there is still a gap between non-noble metal catalysts and commercial Pt/C catalysts in terms of catalytic activity and stability, especially in the acid medium.[3] Non-noble metals can be mainly divided into transition-group metals and main-group (s-block and p-block) metals. Generally, the outer electrons of the main-group metals are non-delocalized, so they lack the combination of empty and filled host-orbitals for multi-electron catalysis, resulting in poor catalytic activity.[5] The atomic structure of transition-group metals, however, can provide unoccupied orbitals or lone pair electrons to reactants, which can successfully lower the activation energy and facilitate the reaction.[2] To this end, great efforts have been devoted to transition metal catalysts. The major concern for non-noble metal catalysts is how to improve the catalytic activity and stability, which makes the catalyst's active site structure a key point to study. In the past few years, there has been an explosion of interest in non-noble metal carbide,[6,7] nitride,[8,9] oxide,[10–12] and phosphide.[13] However, the highest catalytic activity and most widely studied type is M–N–C, which is prepared by high temperature pyrolysis of carbon precursors containing nitrogen and metals.[14,15]

There are some effective approaches to enhance the activities of M–N–C catalysts for the ORR in the current study: (1) regulating the local coordination structure of center metals; (2) doping heteroatoms to adjust the electronic structures of active sites; (3) introducing bimetallic or polymetallic sites; (4) creating more defective-edge M–N–C; (5) increasing exposure of active sites and so on.[3] Herein, we firstly summarized the recent work on the activity sites of non-noble metal catalysts for the acid ORR. Then, we discussed the design and construction of different activity sites and the catalytic mechanisms of these sites in acid medium. We finally concluded with a few suggestions about constructing effective activity sites to facilitate activity and stability for the ORR.

2 Mechanism of acid ORR

The oxygen reduction reaction (ORR) is a complex process that involves multielectron transfer. Nowadays, the ORR reaction paths are mainly divided into the four-electron pathway and two-electron pathway, as shown in Fig. 1.[16]

The related reaction equation is as follows:

Four-electron pathway:

$$O_2 + 4H^+ + 4e^- \rightarrow 2H_2O \quad (1)$$

Two-electron pathway:

$$O_2 + 2H^+ + 2e^- \rightarrow H_2O_2 \quad (2)$$

$$H_2O_2 + 2H^+ + 2e^- \rightarrow 2H_2O \quad (3)$$

$$2H_2O_2 \rightarrow 2H_2O + O_2 \quad (4)$$

For the above two reaction pathways, it is obvious that the two-electron pathway may produce hydrogen peroxide, which can destroy the stability of the catalysts and further reduce the reaction efficiency.[2] In the four electron pathway, the ORR process mainly consist of the following elemental reactions (* represents the catalytically active site):[17]

$$O_2 + * \rightarrow O_2^* \quad (5)$$

Junjie Ge

Prof. Junjie Ge received her Ph.D. in physical chemistry from the Changchun Institute of Applied Chemistry, Chinese Academy of Sciences in 2010. She worked at the University of South Carolina and Hawaii Natural Energy Institute as a postdoc and joined Changchun Institute of Applied Chemistry in March 2015 as a full professor. Her research interests include fuel cells, nanoscience, catalysis, and electrochemistry.

Wei Xing

Prof. Wei Xing is currently the director of the Laboratory of Advanced Power Sources in Changchun Institute of Applied Chemistry. After receiving his Ph. D. in Physical Chemistry, at CIAC in 1995, he worked at the Hong Kong Productivity Council (HKPC). In 2001, he joined CIAC as a professor and devoted his work to development of advanced chemical power sources. His research areas currently involve proton exchange membrane fuel cells from fundamental electro-catalytic processes to relevant fuel cell assembly and testing.

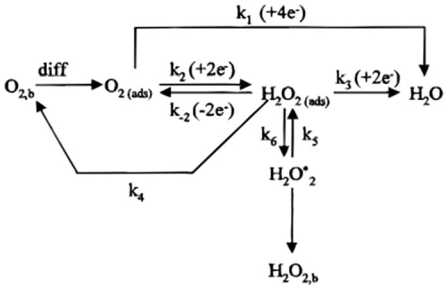

Fig. 1 Schematic diagram of the ORR process under acid conditions.[16]

$$O_2^* + H^+ + e^- \rightarrow OOH^* \quad (6)$$

$$OOH^* + H^+ + e^- \rightarrow H_2O + O^* \quad (7)$$

$$O^* + H^+ + e^- \rightarrow OH^* \quad (8)$$

$$OH^* + H^+ + e^- \rightarrow H_2O + * \quad (9)$$

The whole process includes transfer and coupling of four electrons and four protons, activation and desorption of many reaction intermediates (such as O_2^*, OOH*, O*, and OH*). Generally, we call the slowest step in a reaction the rate determining step (RDS). Different catalysts with different coordination environments will show different RDS. As shown in Fig. 2, the center FeN_4 model and defective-edge FeN_4 model were proposed for DFT calculations (Fig. 2a and b). It clearly shows that several steps are endothermic at the equilibrium potential (U = 1.23 V), and the highest endothermic energy is the formation of OH* for the center FeN_4 model, implying that the RDS is the third electron-transfer step ($O^* + H^+ + e^- \rightarrow OH^*$). By contrast, the last electron-transfer step ($OH^* + H^+ + e^- \rightarrow H_2O + *$) is the RDS for the defective-edge FeN_4 model.[18]

In recent years, in addition to single metallic catalysts, dual-metal catalysts have gradually shown their importance because of their excellent catalytic properties. Dual-metal catalysts can be further subdivided into: bonded dual-metal catalysts and non-bonded dual-metal catalysts. As shown in Fig. 2e and f,[19] the former refers to the fact that the two metals are close enough to form a metal pair, and then coordinate with the surrounding N atoms, which can also be called dual-atomic catalysts (DACs). The latter shows that the two metals are coordinated with N atoms respectively, and the distance between the two metals is far to form metal bonds. Since the configuration of the latter can be simply seen as the combination of two single-metal sites, its reaction mechanism is similar to the mechanism described above. Next, we will focus on the reaction mechanism of bonded dual-metal catalysts. Due to the unique configuration of DACs, three different O_2 adsorption models have been formed, which can be roughly divided into: associative adsorption models (end-on and side-on) and dissociative adsorption models (O_2 decomposes). And it has been found that the adsorption model of oxygen largely determines the reaction pathway of the ORR and even affects the catalytic performance of the catalysts; the schematic diagram of the reaction pathway is shown in Fig. 2g.[20] Obviously, in pathway A, a metal more likely acts as the main active center, while paths B and C show two metals participating in the reaction as active centers at the same time. This involves two reaction mechanisms, modulation mechanism and cooperation mechanism. In the modulation mechanism, one metal in the bimetallic acts as the active center, and the other metal only regulates the electronic structure of the active center. In the cooperation mechanism both metals can adsorb the relevant reaction intermediates, which is expected to break the scaling relationship and exceed the theoretical upper limit of electrocatalytic activity.[21]

Actually, according to the Sabatier principle, ideal catalysts should have a moderate binding energy to the reaction intermediates, which is neither too strong nor too weak. For the ORR, when the adsorption of the active sites to the intermediates is too weak, the proton and electron transfer of oxygen molecules will be restricted. However, if the adsorption is too strong, the product water molecules will closely bond with active sites and prevent oxygen molecules from further adsorption.[22] Some research has demonstrated that the relationship between the catalytic activity of various metals for the ORR and the binding energy of oxygen atoms is represented by a "volcanic plot" curve. Pt locates near the peak of the volcanic plot, which exhibited much better catalytic performance than other non-noble metals for the ORR (Fig. 3a).[23] Fig. 3b shows the volcanic curve of single transition metals supported on graphene to form M–N–C catalytically active sites. The φ, as shown in Fig. 3b, is a descriptor that represents the free-energy for OOH*, O*, and OH* adsorption.[24] The calculation results well matched the experimental results that Fe coordinated with four pyridine N possesses better performance than other transition metals. It further proves that the coordination environment has a great influence on the adsorption energy of intermediates, used for reasonably selecting and designing active sites. Similarly, there is a corresponding volcanic curve relationship for dual-

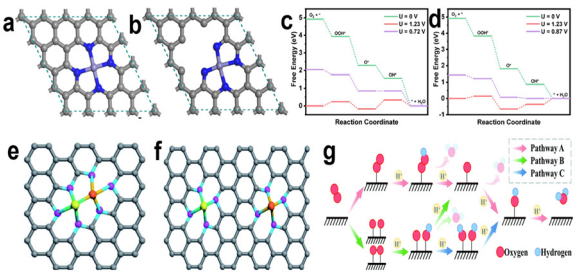

Fig. 2 Model structures used in theoretical studies: (a) center and (b) defective-edge FeN_4 structures. ORR free-energy diagrams of the (c) center and (d) defective-edge FeN_4 structures.[18] Model structure of dual-metal catalysts: (e) bonded dual-metal catalysts and (f) non-bonded dual-metal catalysts.[19] (g) Schematic diagram of the reaction pathway of dual-metal catalysts.[20]

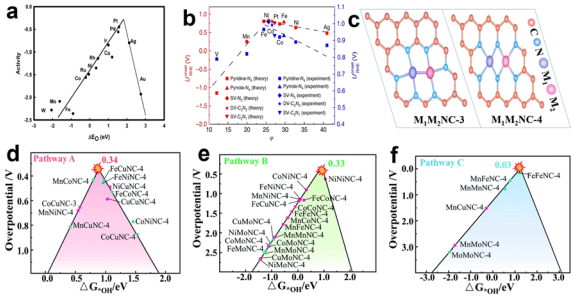

Fig. 3 Volcanic plot relationship (a) between oxygen reduction activity and oxygen binding energy for various metals[23] and (b) between theoretical and experimental onset potentials (U_{RHE}^{onset}) *versus* the descriptor φ for single TM atoms supported on graphene.[24] (c) Structural diagrams of M_1M_2NC-3 and M_1M_2NC-4.[20] (d–f) Volcano plots of the three reaction pathways.[20]

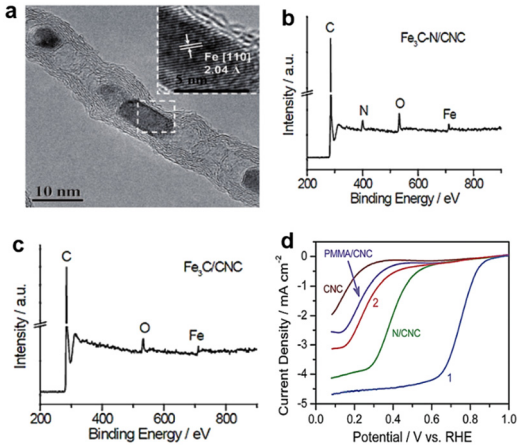

Fig. 4 (a) High resolution transmission electron microscopy (HRTEM) image of Pod-Fe with the inset showing the [110] crystal plane of Fe.[25] XPS spectra of (b) Fe_3C–N/CNC and (c) Fe_3C/CNC.[29] (d) ORR performance of Fe_3C–N/CNC (curve 1) and Fe_3C/CNC (curve 2).[29]

metal catalysts. However, it should be clear that for the same bimetallic catalyst, the catalytic activity of the ORR is related to the choice of ORR pathway. From Zhou *et al.*'s theoretical research on bimetallic oxygen reduction catalysts, they selected two typical active site structures of DACs as simulation objects, and their structural diagrams are shown in Fig. 3c. From the theoretical calculation results, it is found that path C has the smallest limiting potential of 0.03 V by comparing the three reaction paths above (Fig. 3d–f), suggesting that path C is the most thermodynamically active. In addition, for the same bimetallic catalyst such as FeCoNC-4, it presents different overpotentials in path A and path B, which proves that the selection of reaction pathway is important for catalyst activity. Theoretical simulation calculation can help us understand the reaction mechanism simply, and can guide us to quickly design and manufacture catalysts with excellent performance.

3 Single metals as catalytically active site centers

In order to replace Pt-based precious metal electrocatalysts, some efficient active sites with non-noble metals as active centers were designed and synthesized. Combining experimental results and theoretical calculation, Fe and Co-doped carbon electrocatalysts are considered to have a greater competitive advantage compared to platinum-group metals (PGM). So, several typical metal active sites are summarized as follows:

3.1 Fe as active center

Fe-based catalysts for the ORR in acid medium have been well developed after decades of research. Benefiting from characterization technology, we now have a deeper understanding of the configuration of active sites and catalytic mechanism.

Deng *et al.*[25] designed an active and stable catalyst which encapsulated Fe nanoparticles (NPs) into pea-pod like carbon nanotubes (CNTs) to be physically isolated from the acid environment to avoid leaching. The microstructure of the catalyst is shown in Fig. 4a. Even though Fe nanoparticles are wrapped by several layers of carbon sheets, the electrons can transfer from Fe to carbon, which contributes to the decrease of the local work function and strengthens the catalytic activity of the outer CNT shell to promote oxygen reduction.[26] However, there are some questions that need to be solved for this type of catalyst, *i.e.*, which are the real active sites and to what level do those active sites contribute to catalysis? These questions are valid because there are always small amounts of nitrogen and defect vacancies doped into the carbon matrix in the synthesized catalyst. According to previous studies, it can be confirmed that pyridine *N* and vacancy-type defects both exhibit an acidic ORR activity.[27,28] Besides, some iron nanoparticles existed in the catalyst which also have some catalytic activity. In short, the ORR performance of the Fe_3C type of catalyst is the result of multilayer factors and these factors make it difficult to define the specific mechanism of action of the ORR. For example, Sun *et al.*[29] proposed an opposite view that Fe_3C has no ORR catalytic activity. According to the above reports, the materials used to synthesize the catalysts all contain nitrogen sources, such as 1,8-diaminonaphthalene (DAN) and cyanamide. It led to the possibility of forming an Fe-based active center with N participating in the active site structure. The hypothesis was made because high-temperature pyrolysis of the coexisting N-containing source, iron salts and carbon substance can produce Fe/N/C catalysts with abundant Fe–N_x/C moieties.[30–32] In order to explore the influence of the nitrogen source on catalytic performance, the author synthesized two catalysts with or without cyanamide, denoted as Fe_3C–N/CNC and Fe_3C/CNC, respectively. X-ray photoelectron spectroscopy (XPS) spectra demonstrated that N species are present in Fe_3C–N/CNC but not in Fe_3C/CNC (Fig. 4b and c). The ORR performance of the catalysts, as

shown in Fig. 4d, clearly shows that Fe_3C–N/CNC is much better than Fe_3C/CNC. The comparison results indicate that the catalytic activity of pure Fe_3C is not good or even inactive, so, there must exist true active sites, *i.e.* the Fe–N_x/C moieties. Besides, the Fe_3C nanoparticles were usually coated by several layers of carbon film, which may hinder the electron transfer from Fe_3C to the outermost carbon shell and lead to catalyst inactivation. The different results may be derived from differences in synthesis procedures (*i.e.* original material, pyrolysis temperature) and the nature and sensitivity of the characterization techniques utilized.[32] In conclusion, more theoretical calculations and more advanced material synthesis techniques are needed to better understand and enhance the activity of transition metal carbide-based ORR electrocatalysts.[33]

In the 1980s, Yeager's group produced a catalyst by heat-treating polyacrylonitrile (PAN), carbon (Vulcan XC-27) and cobalt/iron acetate which showed promising ORR activity in both alkaline and acid electrolytes.[34] It opens a new way of making ORR catalysts by heat-treating precursors that are composed of the carbon support, nitrogen-containing polymers and metal salts. Since then, the M–N–C type active site has become a hot topic.[35] Lefevre *et al.*[36] synthesized a series of catalysts by pyrolyzing precursors between 400 and 1000 °C, with Fe salts adsorbed on the treated carbon matrix. According to the experimental results, two different catalytic sites simultaneously exist in this series of catalysts, *i.e.*, FeN_4/C and FeN_2/C, and the most representative structures of these sites are FeN_4C_8 and FeN_2C_4, respectively. The formation of the different catalyst structures is temperature dependent. When the pyrolysis temperature is between 500 and 700 °C, N_4-metal bound to the carbon support is easier to form. By contrast, if the pyrolysis temperature ranges from 700 to 900 °C, the quantity of FeN_2/C reaches its maximum, as illustrated in Fig. 5a. The experimental results were measured by Time-of-Flight Secondary Ion Mass Spectrometry (ToF SIMS). It was concluded the variation tendency of three families ($\sum FeN_1C_y^+$, $\sum FeN_3C_y^+$ and $\sum FeN_4C_y^+$) relative intensity with temperature changes, the author deduced the three families belonging to a catalytic site of the FeN_4/C. Fig. 5b shows the possible structure of FeN_2/C. The electrochemical performance was evaluated for these catalysts in H_2SO_4 solution (pH = 1), and the potential V_{pr} represents the maximum reduction occurring at 0 rpm, as shown in Fig. 5c. It demonstrated that the variation tendency of catalytic activity at different temperatures coincided with the change of relative abundance of FeN_2/C. So it can be concluded that FeN_2/C is more active than FeN_4/C, but theoretical calculations reveal the order of ORR activity follows $FeN_4 > FeN_3 > FeN_2 > FeN_1 > FeN_5$.[37] The origin of the difference is that the characterization method is not advanced enough, as some experiments all proved that FeN_4 is the most promising catalytic site.[3] Liu *et al.*[38] used sodium alginate with graphene to immobilize Fe^{3+} cations into a novel structure of "egg-box" (Fig. 5d); subsequent carbonization caused the formation of a N-doped porous

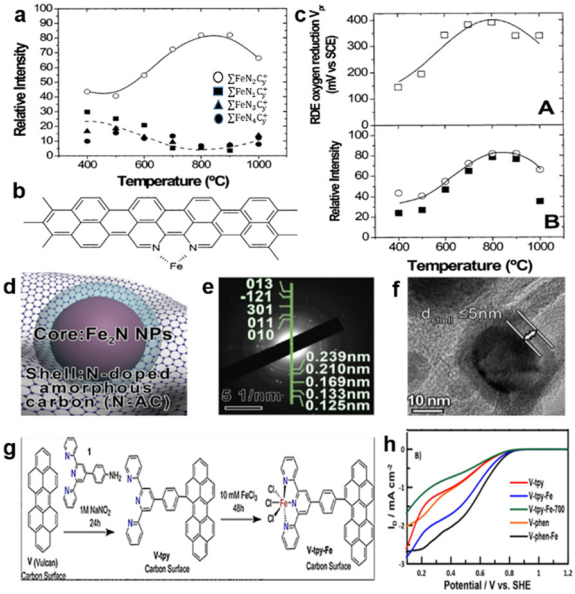

Fig. 5 (a) Relative intensity of different ions of active sites as a function of the pyrolysis temperature.[36] (b) Possible structure of FeN_2/C.[36] (c) The relationship between the catalytic activity (A) and the ToF SIMS relative intensity (B) as a function of the pyrolysis temperature.[36] (d) The structure diagram of "egg-box". (e) The SAED pattern.[38] (f) The HRTEM of encapsulated Fe_2N with thickness shell ≤5 nm.[38] (g) Synthetic diagram of synthesis methodology.[38] (h) RRDE ring currents of different catalysts in 0.1 M H_2SO_4 (the number 700 represents the pyrolysis temperature; phen represents phenanthroline as a raw material to produce N_2/C sites).[39]

carbon shell to encapsulate Fe_2N nanoparticles (NPs). Fig. 5e and f demonstrate that the NPs are Fe_2N, which is coated by a N-doped porous carbon shell with an average thickness of ≤5 nm. The catalyst presented an inferior catalytic activity ($E_{1/2}$, 0.71 V *vs.* RHE) in 0.1 M $HClO_4$ aqueous solution. After 10.5 h of chronoamperometric test, the initial current density had only 19% loss at 0.5 V *vs.* RHE in 0.1 M $HClO_4$ electrolyte. Fruehwald *et al.*[39] used a new way to produce a catalyst with FeN_3/C acting as the active site. The synthetic methodology is shown in Fig. 5g. This method does not necessitate high-temperature pyrolysis to produce the catalyst, and experimental results show that the catalytic performance of materials with heat treatment was worse than the material without pyrolysis (Fig. 5h). The reason for this phenomenon may be the change of the conformation of the active FeN_3/C sites to the inert FeN_{3+3}/C sites, which corresponds with the FeN_2 active sites transforming to another construction of FeN_{2+2} according to a previous report.[32]

According to theoretic prediction and experimental verification, Fe–N–C shows the best catalytic performance among non-noble-metal based catalysts in acid medium.[40] Researchers have synthesized many catalysts with high active site density and high activity by choosing different synthetic materials, regulating the morphology of catalysts, and optimizing the experimental parameters. In previous studies, Fe–N–C type catalysts were primarily synthesized by

pyrolyzing a mixture which consists of a carbon substrate, nitrogen-rich materials, and iron salts, followed by complicated secondary processing.[41] In 2010, Liu *et al.* started to use metal–organic framework (MOF) derived catalysts for the ORR. Employing MOFs as precursors has three main advantages: (1) the characteristic porosity of MOFs can disperse the active sites uniformly after pyrolysis. (2) The properties can be regulated and controlled through rationally designing the structure and morphology of MOFs. (3) MOFs take metals as nodes and are rich in a large number of uniformly distributed metals. In 2011, Dodelet *et al.* adopted ZIF-8 as a carbon and nitrogen source.[42,43] Since then, ZIF-8 has become the most studied material in ORR non-noble metal based catalysts because Zn is easily volatilized at high temperature and can be eliminated during pyrolysis.[44,45] For example, Wang *et al.*[44] prepared a catalyst whose active sites were highly dispersed at the atomic level by doping Fe into ZIF-8 to partially replace Zn ions. They emphasized that an O_2-free environment is crucial for improving the ORR performance, because iron is easily oxidized and aggregated in oxygen-containing environments and a uniform Fe distribution can be more easily achieved at an atomic level in inert Ar atmosphere than in air atmosphere (Fig. 6a). Iron is exchanged as an ion with Zn in ZIF-8 in the process of synthesizing precursors. $Fe^{2+}$and Zn^{2+} have a similar ion radius (cation radii: Fe^{2+} 62 pm and Zn^{2+} 60 pm),[46] but Fe^{3+} has a much smaller radius (49–55 pm), so Fe^{2+} can readily exchange with Zn^{2+}. Besides, Fe^{3+} tends to hydrolyze more than Fe^{2+}, which can be confirmed by similar experimental results for detection of Fe(III) oxide/hydroxide in XPS reported in previous studies (Fig. 6b).[47,48] The catalyst treated in Ar gas has better catalytic performance, with $E_{1/2}$ at 0.82 V *vs.* RHE and H_2O_2 yield as low as 1%. Unfortunately, the stability is poor, with the $E_{1/2}$ negatively shifted by 40 mV after 10 000 cycles. Since Zhang and co-workers demonstrated a novel concept, "single-atom electrocatalysts (SACs)", the high atomic utilization in theory and outstanding catalytic activity of SACs have made them a hot research topic in recent years.[49] Owing to their unique electronic structure, SACs offer the chance to design and regulate the active sites to improve the catalytic performance.[50] However, traditional synthesis methods have some problems in making SACs: (1) to achieve well-defined single-atom dispersion on the carbon support, the concentration of metal atoms must be extremely low, which means the density of active sites is low. (2) A high-temperature pyrolysis process usually leads to aggregation of metal atoms and production of low activity sites, and increasing the content of metal elements will lead to metal aggregation and the formation of low-activity metal nanoparticle aggregation. (3) In most cases, single-atom metals may be faced with the heterogeneous distribution of active sites and a poorly defined coordination environment.[51] After recognizing these issues, great progress thereby has been made in designing Fe-based SACs. For instance, Liu *et al.*[18] synthesized a catalyst with highly dense-FeN_4 single-atom sites, as shown in aberration-corrected high-angle annular dark-field scanning TEM (AC HAADF-STEM) (Fig. 6d). The authors developed a clever method that uses the electrostatic interaction between Fe(II)-phenanthroline (positively charged) and poly-dopamine (PDA) chains (negatively charged) to attach Fe(II)-phenanthroline to PDA, forming the PDA/Fe(II)-phenanthroline complex coated ZIF-8 particles. After carbonization, the catalyst with high-density atomically dispersed Fe–N_4 sites was achieved, as shown in Fig. 6e. PDA not only suppresses the formation of Fe-based aggregates, but also facilitates the formation of meso/macropores, creating abundant defective edge and Fe–N_4 sites for the carbon matrix. Atomically dispersed Fe atoms can also be validated by Fourier-transformed extended X-ray absorption fine structure (FT-EXAFS) characterization (Fig. 6f). And the catalyst exhibits catalytic performance ($E_{1/2}$, 0.828 V *vs.* RHE) which is comparable to commercial Pt/C in 0.1 M $HClO_4$. Besides, there are many other methods to accomplish catalysts for single-atom dispersion of Fe–N_4, such as the silica-protected strategy to realize extraordinary utilization efficiency of Fe,[52] poly(acrylic acid–maleic acid) (P(AA–MA)) copolymer as a chelating agent to chelate with Fe(III) to inhibit iron aggregation,[14] dual melt-salt-mediated template method to avoid rapid loss of nitrogen during pyrolysis and improve Fe–N_4 single-atom site density,[53] and so on.[54–56]

Although these active sites all displayed ORR catalytic performance under certain test conditions, there is still a big gap from practical application of these catalysts. Is there a better catalytic activity when two or more active sites combined their action? A number of studies have confirmed that the synergistic effect between the Fe-based nanoparticles and Fe–N_x configuration can profoundly affect the electron-density distribution of Fe atoms in the center of active sites, which is good for oxygen adsorption and further enhancing the catalytic activity.[57] For example, transition-metal oxides have been studied as electrocatalysts because of their low-cost and chemical stability.[58] Wang *et al.*[59] synthesized a nanofiber catalyst which uniformly distributed Fe_2O_3/FeN_x

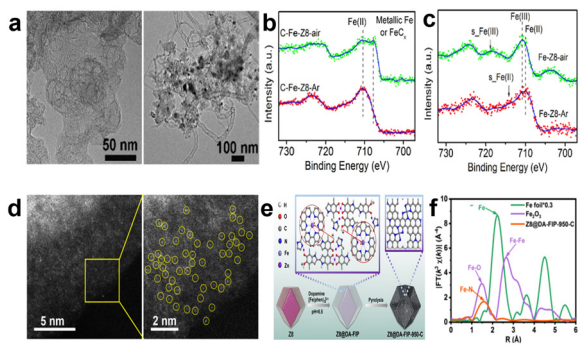

Fig. 6 (a) TEM images of C–Fe-Z8-Ar (left) and C–Fe-Z8-air (right).[44] (b) High resolution Fe 2p XPS spectra of C–Fe-Z8-Ar and C–Fe-Z8-air.[44] (c) XPS spectra of Fe-Z8-Ar and Fe-Z8-air (without carbonization).[44] (d) AC HAADF-STEM images of Z8@DA-FIP-950-C.[18] (e) Illustration of the synthesis of Z8@DA-FIP-950-C.[18] (f) FT Fe K-edge EXAFS spectra of Z8@DA-FIP-950-C and references.[18]

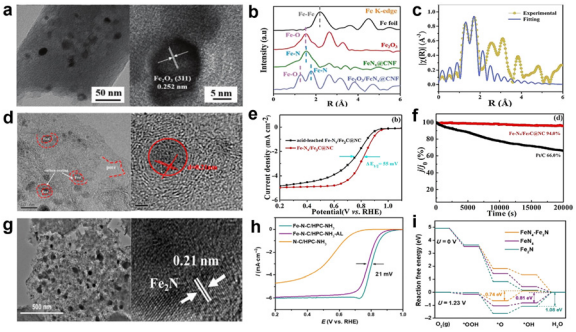

Fig. 7 (a) TEM and HRTEM images of Fe_2O_3/FeN_x@CNF.[59] (b) XRD patterns.[59] (c) FT-EXAFS spectra.[59] (d) TEM and HETEM images of Fe–N_x/Fe_3C@NC.[60] (e) ORR polarization curves of Fe–N_x/Fe_3C@NC and acid-leached Fe–N_x/Fe_3C@NC.[60] (f) Chronoamperometric curves of Fe–N_x/Fe_3C@NC and 20 wt% Pt/C catalysts.[60] (g) TEM images of Fe–N–C/HPC-NH_3 and HRTEM image of the nanoparticle in Fe–N–C/HPC-NH_3.[62] (h) ORR polarization curves.[62] (i) Energy profiles for the ORR over different catalytic sites.[62]

active sites (Fig. 7). It clearly demonstrates that Fe_2O_3 and metallic Fe were absent in the catalyst. According to the Fourier transform Fe k^3-weighted EXAFS (FT-EXAFS) spectra of Fe_2O_3/FeN_x@CNF, the fitting results show that the ratio of N to Fe atoms was 1.8 and O to Fe atoms was 0.2, indicating that the most likely active site of the structure was FeN_2 surrounded by iron oxides. The electrocatalytic performance of the catalyst is much better in alkaline solution than in acid medium, whose $E_{1/2}$ is 0.86 V *vs.* RHE. And the stability is noteworthy due to negligible decay of $E_{1/2}$ which was only 10 mV after 20 000 cycles. In short, the synergistic effect between Fe_2O_3 and FeN_x has a certain impact on the catalytic activity, but the poor performance may be related to the weak conductivity and oxygen adsorption capacity of Fe_2O_3. Xu *et al.*[60] used a cooperative protection strategy to create a catalyst which highly dispersed hyperfine Fe_3C nanodots and abundant Fe–N_x sites (Fe-N_x/Fe_3C@NC). Similarly, Fe_3C nanoparticles are also wrapped by carbon layers as shown in Fig. 7d. The catalyst exhibits an inferior ORR activity; the $E_{1/2}$ is only 0.72 V in 0.5 M H_2SO_4 solution. The synergistic effect can be verified by an acid-leaching catalyst to remove Fe_3C nanodots (Fig. 7e) and adding KSCN solution to poison Fe–N_x sites. These experiments demonstrate that Fe–N_x and Fe_3C are essential for promoting the ORR activity. Fe_3C nanoparticles do not directly participate in the ORR, but they can transfer electrons to the outer graphene shell, thus promoting the activation of oxygen molecules. Although the activity is not good for Fe–N_x/Fe_3C@NC, it has excellent stability that the current density remained 94% after 20 000 s of chronoamperometric test (Fig. 7f), which can be attributed to Fe_3C nanoparticles. It has been reported that crystalline Fe_3C can improve the graphitization degree of the carbon matrix and effectively mitigate carbon corrosion.[61,62] Liu *et al.*[62] heat-treated twice the iron-containing precursors in NH_3 atmosphere to make a catalyst which includes two types of active sites namely FeN_x and Fe_2N, which can be labeled as Fe–N–C/HPC-NH_3, and the morphology of the catalyst is shown in Fig. 7g. NH_3 heat-treatment not only promoted the formation of the Fe_2N nanoparticles, but also increased the porosity and surface area that facilitate the mass transport of reactants and products, further improving the ORR activity. The ORR activity of Fe–N–C/HPC-NH_3 was evaluated in 0.1 M $HClO_4$ solution, the $E_{1/2}$ is 0.803 V and J_m is 1.98 A g^{-1}. In order to investigate the role of Fe_2N nanoparticles, they put the catalyst in 0.5 M H_2SO_4 solution at 80 °C for 12 h to remove Fe_2N, and the $E_{1/2}$ has shifted negatively by 21 mV (Fig. 7h). Besides, DFT calculations were also used to verify that Fe_2N can boost the ORR activity of FeN_x moieties, with results shown in Fig. 7i. An energy barrier of 0.74 eV needs to be overcome for FeN_4–Fe_2N at 1.23 V, which is lower than the single active site of FeN_4 or Fe_2N. This well explains the existence of Fe_2N which lowers the reaction free energy and strengthens the ORR activity of FeN_4.

Moreover, Liu *et al.*[63] synthesized a series of catalysts with close content of FeN_x moieties but different contents of Fe NPs by heating different amounts of iron salts that were doped into pre-carbonized ZIF-8, which were labeled as Fe–N–C-100/300/500, respectively, with the number representing the amount of iron salt added. The morphology of Fe–N–C-300 is shown in Fig. 8a, and those marked with yellow circles represent atomically dispersed Fe atoms. The presence of Fe nanoparticles can be confirmed by XRD and scanning electron microscopy (SEM)/TEM characterization (Fig. 8a and b). The density of FeN_x on the catalyst surface was detected by XPS and the total content of Fe determined by inductively coupled plasma optical emission spectroscopy (ICP-OES); the results are shown in Fig. 8c. It shows that FeN_x contents are similar in the three samples, but the contents of Fe NPs have much difference, which led to different ORR performances. Appropriate content of Fe NPs may produce better activity, and the reason may be that (1) the strong interaction between FeN_x and Fe NPs modifies the electron structure of active centers, which makes the adsorption energy of the reactants/products suitable. (2) Fe NPs assist FeN_x in presenting single atom dispersion, improving the accessibility of FeN_x active sites. (3) Excess Fe NPs may block

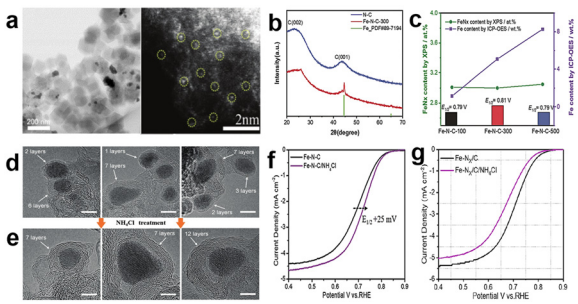

Fig. 8 (a) TEM and HAADF-STEM image of Fe–N–C-300.[63] (b) XRD patterns of the N–C and Fe–N–C-300 catalysts.[63] (c) The data for FeN_x and Fe content by XPS and ICP-OES detection, respectively, and $E_{1/2}$ of Fe–N–C-100/300/500.[63] HRTEM images of (d) the pristine Fe–N–C catalyst and (e) after NH_4Cl-treatment Fe–N–C catalyst. ORR polarization plots of (f) the pristine and NH_4Cl-treated Fe–N–C.[64] (g) NP-free Fe–N_x/C before and after the NH_4Cl treatment.[64]

the FeN_x active sites and result in deceasing activity.[63] However, Chen *et al.*[64] proposed a novel strategy to effectively remove the encapsulated M-NPs by few carbon shells. The acid-leaching method can only remove the exposed M-NPs without carbon encapsulation, but these M-NPs are wrapped by single or few-layers which can't be removed during acid leaching and it is supposed to be active for the ORR. Therefore, it leads to an inability to accurately judge the role of various active sites. So, they used NH_4Cl-treatment to etch out encapsulated M-NPs without destruction of co-existing $M–N_x$ sites. HRTEM showed that the carbon layers of encapsulated Fe-NPs range from single to multiple-layers, but only more than six carbon layer encapsulated Fe-NPs can survive after NH_4Cl-treatment (Fig. 8d and e). Previous theoretical simulations have verified that only less than three or four carbon layers could be modulated by encapsulated M-NPs and enhance the ORR performance.[65,66] Even though there are some Fe-NPs in the catalyst after NH_4Cl-treatment, the recovered Fe-NPs have no ORR activity, so the real catalytic role of M-NPs and $M–N_X$ sites in the ORR can be observed. Fig. 8f shows that the $E_{1/2}$ positively shifted by 25 mV after NH_4Cl treatment, implying that the effect of the encapsulated Fe-NPs was negligible, or even impeded the ORR performance of $Fe–N_x$ sites when there are too many iron nanoparticles in the catalyst. They further researched the mechanism of NH_4Cl-treatment promoting the ORR activity enhancement. Fig. 8g demonstrated that NH_4Cl-treatment would not provide addition nitrogen to form new $Fe–N_x$ sites, but it can remove some M-NPs to improve the specific surface area from 393 to 495 $m^2\ g^{-1}$ and result in more exposed $Fe–N_x$ active sites per unit of mass.

There are many studies reporting that multiplex heteroatom-doped carbon-based catalysts can improve electrocatalytic activity for the ORR.[50,51,67] The light heteroatoms in the nitrogenous carbon matrix, such as O, P, S and B with their suitable electron-donating properties, can generate a potential synergistic effect, which will change the electronic structure of the central metal and regulate the interaction between the metal sites and the ORR intermediates. Li and colleagues synthesized a N, S co-doped carbon-supported catalyst which presented Fe single-atom distribution by pyrolysis of the polyaniline hydrogels containing uniformly distributed Fe precursors.[68] The high-resolution S 2p spectrum of N, S co-doped $C_{PANI–TA–Fe}$ Fe-SA-NC catalysts is shown in Fig. 9a, which shows two major peaks corresponding to C–S–C (S $2p_{3/2}$ at 163.8 eV and S $2p_{1/2}$ at 164.8 eV) and C–SO_x–C (168.13 eV) respectively; there is also a weak peak for S═C–N. Previous studies have confirmed that the presence of C–S–C and S═C–N species can enhance the ORR activity.[69,70] But for the real coordination environment of Fe atoms in N, S co-doped $C_{PANI–TA–Fe}$ Fe-SA-NC catalysts, EXAFS spectroscopy can give the evidence (Fig. 9b). The simulation of the EXAFS reveals that Fe coordinates with four N atoms from the plane and two O atoms from the axial direction (Fig. 9c). The formation of this configuration is due to the chelation between Fe^{3+} and the hydroxyl groups (OH^-) of tannic acid, and O atoms further coordinate with the $Fe–N_4$ moiety to form Fe–O bonds with bridging O_2. N, S co-doped $C_{PANI–TA–Fe}$ Fe-SA-NC exhibited a competitive catalytic activity ($E_{1/2}$, 0.807 V), which can be attributed to the strongly electron-withdrawing N atoms changing the electronic structure of the N-doped carbon materials, making C atoms which are around the N atoms positively charged and promoting the adsorption of oxygen by the catalyst. At the same time, electrons are more easily transferred from the catalyst to the adsorbed oxygen, thereby weakening the oxygen–oxygen bond.[71] Besides, doped S atoms can cause reconstruction of the charge density and spin density of C atoms, and these C atoms with high positive charge density or spin density can serve as catalytically active sites.[72] Some studies demonstrated that the second shell coordination atoms can also impact the electronic structure of Fe–N–C active centers and improve the ORR activity.[73] Yin and colleagues[74] synthesized a catalyst with edge-type FeN_4P_2 sites, as shown in Fig. 9d. The charge density around FeN_4 would be changed after introducing P atoms into the carbon-based matrix and the adsorption energy of intermediates regulated. FT-EXAFS curves show that no apparent peaks of Fe–Fe coordination (2.20 and 4.42 Å) have been found (Fig. 9e), confirming the iron single-atom distribution. Fig. 9e shows the Raman spectra of Fe–N–C–P/N, P–C and Fe–N–C/N–C; the D band (1350 cm^{-1}) and G band (1585 cm^{-1}) represent the degree of defect and graphitization of the carbon substrate, respectively. The value of I_D/I_G for Fe–N–C–P/N, P–C is higher than Fe–N–C/N–C, which revealed that the introduction of P created more defects. Besides, Fe–N–C–P/N, P–C has a smaller C–N content by comparing the results of XPS with Fe–N–C/N–C. Combining the experiments, doping P can help form single-atom Fe and generate more

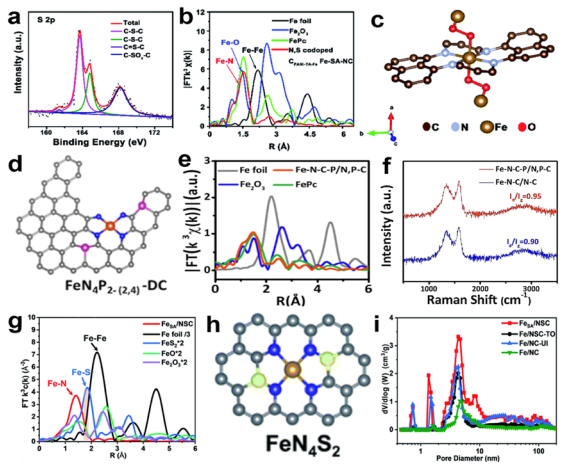

Fig. 9 (a) High-resolution XPS spectra of S 2p.[68] (b) Magnitudes of k^3-weighted Fourier-transformed EXAFS data of Fe atoms.[68] (c) The structure of the active site in N, S co-doped $C_{PANI–TA–Fe}$ Fe-SA-NC.[68] (d) Schematic diagram of the edge-type FeN_4P_2 site.[74] (e) FT-EXAFS curves of Fe–N–C–P/N, P–C and reference materials.[74] (f) Raman spectra of Fe–N–C–P/N, P–C and Fe–N–C/N–C.[74] (g) FT-EXAFS spectra of Fe_{SA}/NSC and other references.[75] (h) Model of FeN_4S_2.[75] (i) Pore size distribution curves of Fe_{SA}/NSC and other catalysts.[75]

edge FeN_4 moieties. Moreover, the DFT calculations reveal that the edge-type FeN_4P_2 site is more active than in-plane type FeN_4P_2. Similarly, Liu *et al.*[75] synthesized a N, S-co-doped hierarchically ordered porous catalyst (Fe_{SA}/NSC) using thiourea as a sulfur source and dopamine as a nitrogen source. The active site construction of Fe_{SA}/NSC was confirmed by DFT calculations and EXAFS spectra (Fig. 9g), which attests that Fe only coordinates with N atoms, not with S atoms. The schematic diagram of the structure is shown in Fig. 9h, where Fe is the center atom, four N atoms are in the first coordination shell and two S atoms are in the second shell. Thiourea was introduced as a S source and nitrogen source to anchor more Fe atoms and increase the active site density. Besides, thiourea plays a pivotal role in improving the Brunauer–Emmett–Teller (BET) surface area and constructing the hierarchically ordered porous carbon structure during the process of high-temperature pyrolysis. The BET surface area of Fe_{SA}/NSC (1224.03 m^2 g^{-1}) is much higher than that of Fe/NC-UI (1091.34 m^2 g^{-1}) synthesized without a S source. Moreover, Fe_{SA}/NSC exhibits a wider pore size distribution than other catalysts (Fig. 9i), and the hierarchically porous structure is beneficial for boosting the performance of the ORR. It can be attributed to the fact that thiourea could break down and produce a large number of bubbles in the pyrolysis process. In summary, the introduction of sulfur atoms can tune the coordination environment of Fe–N_4 and improve the catalytic activity. Besides, other heteroatoms (such as F and B) doped in the nitrogen-containing carbon support can also change the electronic structure of active sites, which benefits the ORR.[76–79]

3.2 Co as active center

Although Fe-based catalysts especially Fe–N_4 are the most likely alternative to commercial Pt/C, their poor stability is still a big problem that needs to be overcome. The main factor affecting the stability of Fe-based catalysts is the Fe-related Fenton reaction that easily produces strong oxidizing radicals, which can cause carbon support oxidation and destroy Fe–N–C active sites. However, Co-based catalysts with a weak Fenton reaction can readily improve the stability, and the catalytic activity of Co–N–C catalysts is comparable to that of Fe–N–C catalysts, so Co is considered an ideal active center.

Yan *et al.*[80] synthesized a bamboo-like carbonitride nanotube catalyst which consists of multi-type active sites, such as encapsulated Co nanoparticles, intercalated CoO species, and Co–N_x coordination sites. Fig. 10a shows the XRD patterns of the CoO@Co–N-bCNT samples synthesized at different temperatures. They proved that melamine would decompose into NH_3 and NO_2 and at the same time, $CoCl_2$ decomposes and forms cobalt oxides from 300 to 500 °C by using thermal analysis. When the temperature is above 600 °C, the cobalt oxides were restored to metallic Co and the Co catalyzed the decomposition of carbonaceous species to form carbon nanotubes.[81–83] The main form of Co atoms in the catalyst is metallic Co, as shown in Fig. 10b. There is a dominant peak at 2.18 Å which demonstrates the Co–Co bond and two weak peaks at 1.53 Å and 1.12 Å, respectively, corresponding to Co–N_x and Co–O structures. Experiments shows that the half-wave potential is positively correlated with the content of Co–N_x sites (Fig. 10c), which demonstrates that Co–N_x sites play pivotal roles in all active sites for the ORR. But the content of Co–N_x sites is unconsidered, which ultimately leads to poor activity. He *et al.*[84] achieved high density atomically dispersed Co doped into the carbon support *via* a surfactant-assisted metal–organic-framework approach. The surfactant coordinated with Co^{2+} and Zn^{2+} to form a protective layer around the surface of ZIF-8, and the surfactant layer first underwent carbonation, forming a carbon shell on the Co-ZIF-8 surface during the pyrolysis. The carbon shell led to a unique confinement effect, which prevented the aggregation of neighboring Co single atoms and mitigated the collapse of internal microporous structures derived from Co-ZIF-8.[85,86] The authors proposed a more likely active site structure of CoN_{2+2} sites as shown in Fig. 10d for the Co–N–C@F127 catalyst. It's not likely that the general CoN_4 moiety embedded in intact graphitic layer, CoN_{2+2} site is a CoN_4 moiety bridging over two adjacent armchair graphitic edge. It can be proved by FT-EXAFS fitting results (Fig. 10e), and the fitted Co–N bond length was 1.94 ± 0.2 Å, but according to the theoretical calculations, the Co–N bond length is 1.85 Å and 1.88 Å of CoN_4 and CoN_{2+2} sites, respectively. Besides, DFT calculations were also used to evaluate the possible structure (Fig. 10f). The free energy evolution diagram for CoN_{2+2} sites shows a downhill trend under a limiting electrode potential of U = 0.73 V, which indicates that CoN_{2+2} sites are thermodynamically capable of catalyzing the $4e^-$ ORR. But for CoN_4 sites, there is an energy barrier that needs to be overcome, and it suggests that CoN_4 sites do not follow the four-electron path for the ORR. It can be verified that the

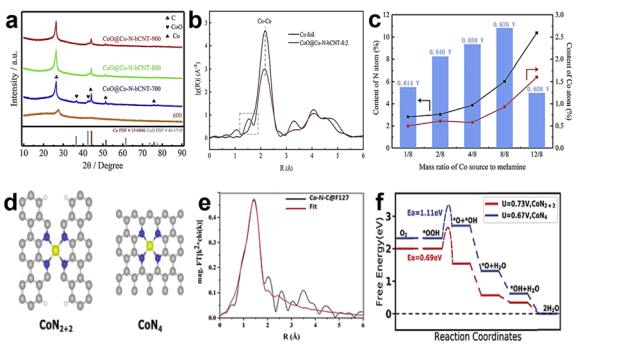

Fig. 10 (a) XRD patterns of CoO@Co–N-bCNT samples synthesized at different temperatures.[80] (b) Co K-edge EXAFS spectra of CoO@Co–N-bCNT-8 : 2 (8 : 2 is mass ratio of Co source to melamine) and Co foil.[80] (c) Relationship among $E_{1/2}$, N content and Co content of the CoO@Co–N-bCNT samples.[80] (d) Structure of CoN_{2+2} and CoN_4 active sites.[84] (e) The fitted spectra of FT-EXAFS for the Co–N–C@F127 catalyst.[84] (f) Free energy evolution diagram for the $4e^-$ ORR pathway on the CoN_{2+2} and CoN_4 active sites.[84]

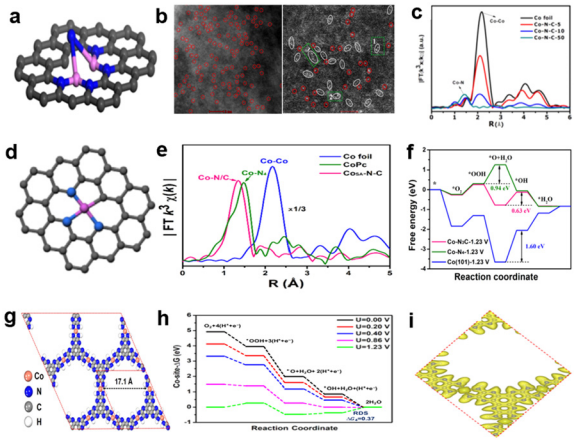

Fig. 11 (a) Schematic structure of Co_2N_5/C, Co(purple), N(blue), C(gray).[89] (b) Aberration-corrected HAADF-STEM images of Co–N–C-50 (left) and Co–N–C-10 (right).[89] (c) FT-EXAFS spectra.[89] (d) Schematic structure of Co_{SA}–N–C, Co(pink), N(blue), C(grey).[90] (e) FT-EXAFS curves of Co_{SA}–N–C and references.[90] (f) Free energy paths of the ORR on Co–N_3C, Co–N_4 and Co at U = 1.23 V.[90] (g) The structure of $Co_3(HADQ)_2$.[91] (h) The free energy diagrams of the ORR for $Co_3(HADQ)_2$ at different potentials.[91] (i) Charge density distribution of $Co_3(HADQ)_2$.[91]

Co–N–C@F127 catalyst follows the $4e^-$ reduction pathway by electrochemical testing. So, the above experiments prove that the dominate active sites are CoN_{2+2}. And the Co–N–C@F127 catalyst exhibited an $E_{1/2}$ of 0.84 V *vs.* RHE in 0.5 M H_2SO_4, which is comparable most Fe–N–C catalysts. Moreover, some researchers used appropriate methods to synthesise catalysts with single-atom dispersed high-density CoN_4 active sites, which also exhibit good activity in the acid environment.[87,88]

Xiao *et al.*[89] firstly detected binuclear Co_2N_x sites and eventually confirmed the structure of Co_2N_5 by DFT calculation; the structure diagram of Co_2N_5/C is shown in Fig. 11a. The formation of binuclear Co_2N_5 sites can alter the atomic ratio of Zn/Co in the process of preparing the catalyst. For example, when the atomic ratio is 50, there are only single atom CoN_x sites in Co–N–C-50, but for Co–N–C-10 (atomic ratio is 10), there are both single atom CoN_x sites and binuclear Co_2N_5 sites with Co–Co distance at 2.1–2.2 Å, as shown in Fig. 11b. It can be noted that the Co–N coordination peak of Co–N–C-10 positively shifts compared with Co–N–C-50, which reveals that there are no pure CoN_x sites in Co–N–C-10, but other sites. There is a special peak at 2.12 Å corresponding to the bimetallic atom structure, consistent with the aberration-corrected STEM in Co–N–C-10. These all confirmed the presence of special Co_2N_5 sites. The high activity was achieved on Co–N–C-10 with a half-wave potential of 0.79 V, and the catalytic activity of the Co_2N_5 site is approximately 12 times higher than the conventional CoN_4 site by quantifying the atomic percentage of Co particles and simple calculations. This study demonstrated that the high activity of bimetallic sites has potential to further improve the catalytic performance, which inspired further exploration of bimetallic catalysts to improve the catalytic performance. Zhou *et al.*[90] synthesized a single-atom distributed catalyst (Co_{SA}–N–C) with active site structure of Co–N_3C, as shown in Fig. 11d. The structure was verified by least-squares EXAFS fitting, the EXAFS fitting coordination number of Co was about 4, and one Co atom was coordinated with three N atoms and one C atom. Cobalt phthalocyanine (CoPc) as a reference also demonstrated that the active site structure in Co_{SA}–N–C isn't like with Co–N_4 (Fig. 11e). CoPc has a typical Co–N_4 structure, and the characteristic peak is at 1.48 Å, but for Co_{SA}–N–C, the dominant peak is at approximately 1.4 Å; the shorter length of Co_{SA}–N–C can be attributed to the carbon atom replacing the nitrogen atom. The greater activity of Co–N_3C sites than Co–N_4 sites was proved by DFT calculation. Fig. 11f shows the free energy paths at U = 1.23 V, and the activation energy barrier is 0.94 eV for Co–N_4, corresponding to the process of the reduction of *OOH to *O. It's much higher than Co–N_3C (0.63 eV) to drive the reduction of *O to *OH, which suggests that Co–N_3C can decrease the activation energy barrier of the rate determining step to accelerate the ORR process compared with conventional Co–N_4. The linear sweep voltammetry (LSV) curves show that the $E_{1/2}$ is 0.79 V of Co_{SA}–N–C, which can compete with Pt/C (0.805 V) in 0.1 M $HClO_4$. Moreover, Iqbal and colleagues[91] used a novel strategy without the need for high temperature pyrolysis to synthesize a catalyst with high catalytic performance. The methodology was inspired by a computational study that indicated the pristine 2D metal hexahydroxybenzene framework as catalytic for the ORR in acid media.[92] In addition, the pyrolysis method can damage the well-defined structure of the MOF and the pristine 2D MOF is highly conductive.[93,94] So, the researchers created a novel cobalt based 2D conjugated MOF catalyst by a hydrothermal reaction, and the resulting catalyst is labeled as $Co_3(HADQ)_2$. There is also a novel active site structure of $Co(NH)_4$, as shown in Fig. 11g. The catalyst exhibited good activity and stability, the $E_{1/2}$ is 0.825 V and the current density degraded by only 5.4% after 20 000 cycles. The high activity of $Co_3(HADQ)_2$ was also confirmed by DFT calculations (Fig. 11h), and the activation energy barrier of the RDS is only 0.37 eV at U = 1.23 V, which is smaller than other active sites. The reasons for the high performance of $Co_3(HADQ)_2$ can be summarized in the following aspects: (1) single Co atom distribution. The nearest distance between two Co atoms is 11.01 Å, which ensures that it's impossible for Co atoms to aggregate and improves the utilization ratio of active sites. (2) Porous structure. As shown in Fig. 11g, the pore size of $Co_3(HADQ)_2$ is 17.1 Å, and this unique construction increases the chance of the active site contact with the reactants and facilitates the ORR process. (3) High electrical conductivity. Because of the high electron delocalization between the CoN_4 motifs, $Co_3(HADQ)_2$ is highly conductive as shown in Fig. 11i.

According to the DFT calculation, Co_9S_8 has catalytic activity similar to Pt/C *via* a four-electron pathway for the ORR, which suggests that cobalt sulfides have the potential to replace the commercial Pt/C. From this, Wang and colleagues[95] synthesized a novel cobalt sulfide-graphene

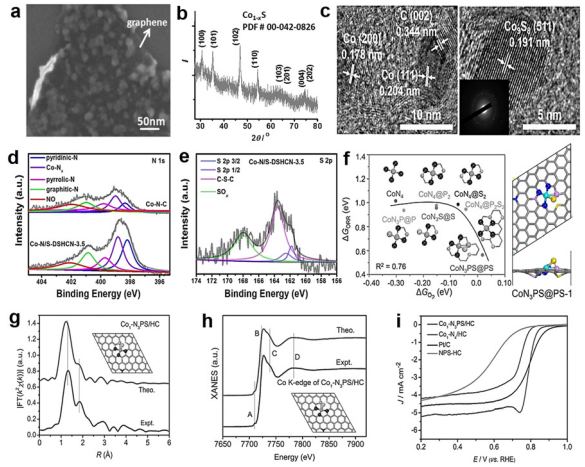

Fig. 12 (a) High-magnification SEM image of $Co_{1-x}S$/RGO.[95] (b) XRD spectra of $Co_{1-x}S$/RGO.[95] (c) HRTEM of Co–N/S-DSHCN, inset is the corresponding SAED pattern of Co-N/S-DSHCN.[96] High-resolution XPS spectra of (d) N 1s. (e) S 2p.[96] (f) The relationship between ORR activity (ΔG_{ORR}) and O_2^* adsorption energy (ΔG_{O_2}) at U = 1.23 V and structural model of CoN_3PS.[101] (g) Comparison between the experimental and theoretically simulated FT-EXAFS spectra of CoN_3PS/HC.[101] (h) Comparison between the experimental and theoretically simulated XANES spectra of CoN_3PS/HC.[101] (i) Polarization curves of CoN_3PS/HC and references in 0.5 M H_2SO_4.[101]

hybrid electrocatalyst (Fig. 12a). The catalyst was verified as $Co_{1-x}S$ nanoparticles grown on reduced graphene oxide (RGO) (Fig. 12b). $Co_{1-x}S$ acts as a connector to link RGO sheets together, and the $Co_{1-x}S$/RGO hybrid catalyst forms a conducting network to accelerate the transfer of electrons and facilitate the ORR activity. Furthermore, Wang *et al.*[96] synthesized a dual-shelled Co, N, S co-doped hollow carbon nanocage catalyst which includes Co_9S_8 nanoparticles, denoted as Co–N/S-DSHCN. There are other active sites except Co_9S_8, such as Co–N_x and metallic Co nanoparticles coated with several graphitic shells, which can also be proved by advanced characterization techniques and jointly drive the performance improvements for the ORR (Fig. 12c). According to the experiments, S doping can improve the catalytic performance, which can be attributed to the following aspects: (1) doping S into the nitrogen-containing carbon substrate increased the contents of the pyridinic-N, graphitic-N and Co–N_x, as shown in Fig. 12d. The pyridinic-N and Co–N_x are the key factors to reduce the ORR overpotential and graphitic-N has a great influence in limiting the current density, which has reached a broad consensus.[97] (2) Doping of S introduces more sulfur-based active sites (Fig. 12e). These two prominent peaks belong to C–S–C (163.6 eV) and high-spin-density C–SO_x^{n-} (168.0 eV), and the other weaker peaks intrinsically originate from Co_9S_8. A previous study has shown that these S-containing species can facilitate the ORR performance.[98] Combining the above analysis, Co–N/S-DSHCN is more active than Co–N–C. Some studies proved that the symmetrical planar structure may lead to limited ORR kinetics inhibiting the adsorption and activation of the ORR-related species.[99,100] In order to explore better catalytic performance, Chen *et al.*[101] estimated P and S co-doped ORR materials, which exhibited excellent ORR performance by DFT calculations. The result shows that the CoN_3PS@PS model exhibits the best ORR performance, as shown in Fig. 12f. The curve shows that the CoN_3PS@PS model exhibits the highest activity (η = 0.58 eV) and lowest ΔG_{O_2} (0.02 eV). They then synthesized a catalyst with atomically dispersed Co species and the main active site is CoN_3PS; the specific structure of the active site is shown in Fig. 12f. According to the least-squares EXAFS curve-fitting analysis, the number of N, P, and S that coordinate with Co is 3.1, 0.9, and 1.1, respectively, which verifies that the synthetic catalyst contains the CoN_3PS moieties. Comparisons between theoretical simulation and experimental results of FT-EXAFS (Fig. 12g) and X-ray absorption near edge structure (XANES) (Fig. 12h) spectra were also presented. These figures all show that the experimental spectra are in good agreement with the theoretical simulation. As shown in Fig. 12i, the acidic ORR performance of CoN_3PS/HC was evaluated, and the $E_{1/2}$ of CoN_3PS/HC similar to commercial Pt/C. But the kinetics current density (J_K) of CoN_3PS/HC is better than that of Pt/C, suggesting that the CoN_3PS/HC catalyst has better kinetic activity than commercial Pt/C.

3.3 Other single-metals as active centers

Although Fe–N–C catalysts reflect excellent ORR activity in acid medium, their stability has always bothered investigators. It seems that Co–N–C catalysts are promising to replace Fe because of their lower Fenton reactivity, but actually the electrocatalytic performance of Co–N–C catalysts is usually inferior to that of Fe–N–C in acid medium. Besides, a big problem for Co–N–C catalysts is that Co-based catalysts tend to produce undesirable hydrogen peroxide by the two-electron transfer pathway. Many studies have reported that the selectivity of Co–N–C catalysts to hydrogen peroxide is more than 90%.[102] In fact, the intermediate H_2O_2 of the two-electron pathway may damage the catalyst and proton exchange membrane, so the two-electron pathway is not expected to happen. Hence, seeking other non-noble metals as active centers is necessary.

For example, Li *et al.*[103] synthesized a single atom Mn–N–C catalyst which reached an $E_{1/2}$ of 0.80 V in 0.5 M H_2SO_4, owing to the Mn–N_4 active sites. The catalyst formed by Cr also has some catalytic activity. Luo *et al.*[104] proposed a Cr–N–C single-atom catalyst where the active site is Cr–N_4 configuration, displaying an $E_{1/2}$ of 0.761 V. It can be seen that the catalysts with transition metal as the active center are mostly studied at present. Besides, recent attempts have been made to study catalysts with main group metals as active centers. However, main group metals are generally considered to have low catalytic activity or even inactive for the ORR. The reason for this is that main group metals lack empty host-orbitals for electrons to occupy, so it's hard for them to participate in the electron transfer process in the catalytic reaction, especially for the ORR which involves

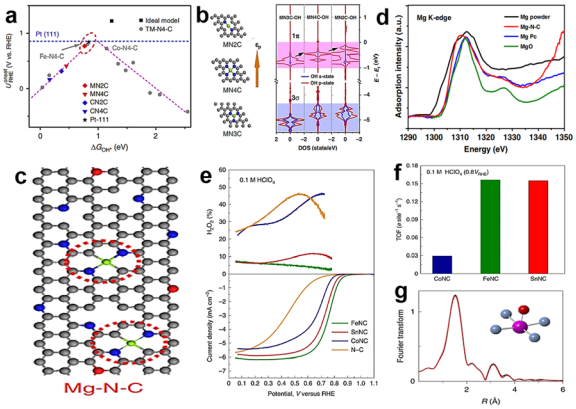

Fig. 13 (a) The relationship between the onset potential and ΔG_{OH*} of different catalysts.[5] (b) The structure of different Mg–N–C coordination environments which tune the ε_p of Mg atoms and the corresponding density of state changes of OH after interaction with the p-state of Mg.[5] (c) Microstructural diagram of Mg–N–C.[5] (d) The XANES of Mg K-edge of Mg–N–C and references.[5] (e) The yield of H_2O_2 (top) and ORR polarization curves of different catalysts (bottom).[105] (f) Comparison of TOF values at 0.8 V_{RHE}.[105] (g) Fourier-transform EXAFS spectrum of SnNC; the black curve is the experimental spectra and the red curve is the theoretical spectra.[105]

multi-electron transfer. The tunable electronic properties of single atom catalysts have provided tunable activities to the main group centers within the bounds of possibility. Liu *et al.*[5] predicted that MgN_2C is a promising active site because the MN_2C model is located near the top of the volcano map with moderate oxygenated species adsorption strength (Fig. 13a). It can be clearly seen that MN_4C (M = Mg, Al, Ca) is located at the left side of the volcano map, which suggests strong adsorption of OH*. The coordination environment can adjust the electron filling of the 3p orbital of Mg centers, as shown in Fig. 13b. It is clear that the p-band center position (ε_p) of MgN_2C sites is the highest and the density of states (DOS) of OH (especially 1π) after interaction with the p-state of Mg is higher, which means weak adsorption and higher catalytic activity. Therefore, main-group metals can also have catalytic properties similar to those of d-band metals by appropriate coordination environment regulation. According to this prediction, they synthesized a catalyst with MgN_2C moieties (Fig. 13c), which exhibited good electrocatalyst activity and better stability than Pt/C. Fig. 13d shows the XANES of Mg K-edge curves, and the pre-edge of Mg–N–C coincides with MgPc, which means that the valance state of Mg is between 0 and +2, but the edge of Mg–N–C is left shifted compared to MgPc, suggesting that the coordination number of Mg–N in Mg–N–C should be less than 4. DFT calculation results show MgN_1C is unstable and MgN_3C is less reactive, so the most likely structure is MN_2C. Moreover, Luo *et al.*[105] prepared Sn–N–C which exhibited inferior activity and selectivity for the four-electron reduction pathway to Fe–N–C, but the turn-over frequency (TOF) is similar, which demonstrates that the intrinsic reactivity of Sn–N–C is comparable to that of Fe–N–C (Fig. 13e and f). According to the Fourier-transformed EXAFS spectrum (Fig. 13g), the Sn atom coordinated with four in-plane N atoms and one axial O atom. These research studies demonstrated the main-group metals are likely to be catalytically active centers, which broadens the design idea of non-precious metal catalysts for the ORR.

4 Dual metals as catalytically active site centers

Since single atomic sites have such good properties, would adding another metal improve their properties? It has been found that the O_2 molecule is attached to a single-atom site through the side-on or end-on model. But different from single-metal doping, O_2 tends to adsorb on a dual-metal site by the bridge-*cis* model, thus the strength of the oxygen bond will be weakened.[106,107] If dual-metals are introduced, the synergistic catalytic effect between metals can adjust the electronic structure of active sites and further improve the performance for the ORR. Inspired by the above discovery, designing and synthesizing dual-metal site catalysts have aroused great interest. Dual-metal catalysts can be divided into two main types: one is where the active part consists of a simple superposition of two kinds of active sites with different center metals, because the two metals are far enough apart that they are not bonding. The other is where the two metal atoms are close to form a bond and generate electronic interaction, which can promote the intrinsic catalytic activities.[2,3,50]

4.1 Fe–Co dual-metal as active center

Hu *et al.*[108] studied the catalytic activity and stability of different active sites by density function theory calculations, including three types of sites: $FeCoN_6$, $FeCoN_7$ and $FeCoN_8$. It can be verified that introducing the second metal atom can

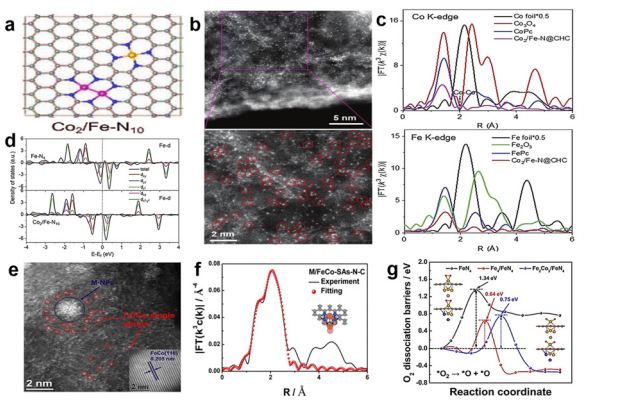

Fig. 14 (a) The structure diagram of Co_2/Fe–N@CHC.[109] (b) Aberration-corrected HAADF-STEM images of Co_2/Fe–N@CHC.[109] (c) FT-EXAFS spectra of Co K-edge (top) and Fe K-edge (bottom) of Co_2/Fe–N@CHC and references.[109] (d) The projected density of states (PDOS) of Fe-d orbitals in FeN_4 (top) and Co_2/Fe–N@CHC (bottom).[109] (e) Aberration-corrected HAADF-STEM images of M/FeCo-SAs-N–C, inset is the HR-STEM of an individual particle.[110] (f) Fe K-edge EXAFS experimental and fitting curves.[110] (g) O_2 dissociation barriers on Fe–N_4, Fe_4/Fe–N_4 and Fe_2Co_2/Fe–N_4.[110]

greatly improve the stability and ORR activity. These studied catalysts are all stable, but the catalytic activity of type $FeCoN_6$ is lower than that of $FeCoN_7$ and $FeCoN_8$, which is attributed to the excessive adsorption strength between active sites and reaction intermediates. In theory, the top site of the Co atom is more likely to be the active center, as the overpotentials of the top site of Co atoms are all lower than the top site of Fe atoms. The internal mechanism of improving the performance of Fe–Co–N–C is that the introduction of the second Fe atom can increase the binding strength between Co and atomic O. Therefore, Fe–Co–N–C catalysts are a promising alternative for Pt-based catalysts.

Wang *et al.*[109] prepared a new catalyst which concludes two types of sites, Co_2N_6 and FeN_4, and the configuration of the catalyst is shown in Fig. 14a. The aberration-corrected HAADF-STEM verified the coexistence of the two types of sites, and it clearly shows that single-atom sites and dual-atom sites correspond to the configurations of FeN_4 and Co_2N_6, respectively (Fig. 14b). Moreover, they employed Fourier-transformed EXAFS to further investigate the coordination environment of Co and Fe in Co_2/Fe–N@CHC, as shown in Fig. 14c. The spectrum of Co K-edge in Co_2/Fe–N@CHC shows a weak peak at about 2.1 Å, which confirms the existence of Co–Co coordination. On the contrary, the spectrum of Fe K-edge in Co_2/Fe–N@CHC does not have a special peak associated with Fe–Fe. And the Co and Fe K-edge EXAFS fitting result also indicated that the Co species have three N and one Co neighbor, while the Fe species coordinate with four N atoms, which also demonstrated the coexistence of Co_2N_6 and FeN_4. There is no doubt that Co_2/Fe–N@CHC exhibited good activity, and the $E_{1/2}$ reached 0.812 V in 0.1 M $HClO_4$, which is better than Co_2–N_6@CHC (0.770 V) and Fe–N_4@CHC (0.787 V). This result suggests that the coexistence of two different active sites can greatly improve the catalytic performance. In order to explore the internal mechanism of activity enhancement, they next carried out DFT theoretical simulation calculation. The calculation results displayed that the property of Co_2–N_6 sites was inferior to that of Fe–N_4 sites, so Co_2–N_6 sites play an auxiliary role to Fe–N_4 sites. It is obvious from Fig. 14d that there is a significant negative shift in the d-band center of Fe after introducing Co_2–N_6 sites, resulting in an increased antibonding orbital filling, which weakens the adsorption strength of the Fe-center and reaction intermediates. Moreover, Yin *et al.*[110] prepared a new FeCo–N–C catalyst (M/FeCo-SAs-N–C) which contains metal nanoparticles (M-NPs) and M–N_4 composite sites. The special structure of composite sites is shown in Fig. 14e; the bigger cluster represents FeCo NPs, which can be confirmed by the lattice distance of 0.205 nm (inset of Fig. 14e). Single Fe/Co atom sites were marked in red circles. The specific coordination environment was evaluated by Fe K-edge EXAFS fitting results (Fig. 14f), and the coordination numbers of Fe–N and Fe–Fe were about 4 and 2, respectively, which suggests the coexistence of M-NPs and M–N_4. It exhibited the best catalytic performance compared with Co-SAs-N–C, Fe-SAs-N–C and FeCo-SAs-N–C in

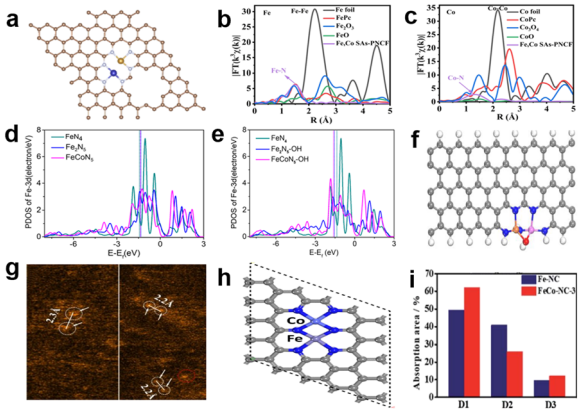

Fig. 15 (a) The schematic structure of Fe, Co SAs-PNCF.[111] FT-EXAFS spectra of (b) Fe K-edge and (c) Co K-edge.[111] Fe 3d PDOS (d) before and (e) after absorption of OH*.[15] (f) The structure of $FeCoN_5$-OH site.[15] (g) AC HAADF-STEM images of $FeCoN_x$/C.[15] (h) The main active site structure of FeCo-NC-3.[113] (i) The content of three Fe moieties which comes from the analysis of Fe Mössbauer spectroscopy.[113]

0.1 M $HClO_4$, which can be attributed to the synergistic effect between M-NPs and M–N_4, owing to the lower dissociation barrier of O_2 on composite sites than Fe–N_4 (Fig. 14g). The internal synergistic effect mechanism can be summarized as follows: a partial electron transfer from M-NPs to Fe–N_4 increases the charge density of the adsorbed O_2 molecule, which leads to the O–O bond length being elongated and reduces the barrier of O_2 dissociation.

In the case where Fe and Co atoms are close enough to produce a synergistic effect, Jiang *et al.*[111] proposed a new active site structure of N_3–Fe–Co–N_3, as shown in Fig. 15a. The special structure can be proved by FT-EXAFS and corresponding fitting results; the FT-EXAFS of Fe K-edge and Co K-edge are presented in Fig. 15b and c, respectively. It is notable that there are two obvious peaks respectively corresponding to Fe–N (1.50 Å) and Co–N (1.32 Å) coordination environment, and a peak at about 2.30 Å that indicates the existence of Fe–Co bonds.[112] The distance is in agreement with HAADF-STEM images, which is about 0.23 nm between Fe and Co atoms. The concrete coordination paths of Fe–N, Co–N and Fe–Co can be calculated by FT-EXAFS fitted curves based on DFT simulations. Eventually, the coordination numbers of Fe–N, Co–N, Fe–Co and Co–Fe are approximately 2.84, 2.89, 0.86 and 0.8, respectively. These results well verify the correctness of the N_3–Fe–Co–N_3 configuration. The catalyst achieved an unremarkable performance in the acidic solution, but its performance exceeds commercial Pt/C in alkaline environment. The reason for the ORR catalytic performance may be the synergetic effect of Fe–Co dual-atom sites and abundant atomically dispersed N_3–Fe–Co–N_3 sites. Xiao *et al.*[15] then constructed an Fe–Co dual-atom centered site to greatly enhance the ORR activity. Firstly, they carried out DFT calculations to investigate the thermodynamic stability and intrinsic mechanism of the catalytic activity of the dual-metal center. The Fe 3d partial density of states (PDOS) is shown in

Fig. 15d and e, and it can be clearly seen that the d-band center of dual-atom centered structures has undergone a slight positive shift compared with the single-atom centered site, which means stronger adsorption of ORR intermediates on the dual-atom centered sites. It indicates that intermediates are more likely to adsorb stably onto dual-atom centered sites. In the process of the ORR, water will spontaneously decompose and the OH* generated can be stabilized on $FeCoN_5$ to form a new $FeCoN_5$–OH site; the structure is shown in Fig. 15f. The d-band center of the new $FeCoN_5$–OH site has a significant negative shift compared to the FeN_4 site (Fig. 15e). According to the d-band center theory, the d-band center's negative shift can lead to an increase in the filling degree of anti-bonding orbitals, which weakens the binding strength between the active sites and intermediates and improves the catalytic performance. Guided by theoretical calculations, a catalyst with the $FeCoN_5$ site was synthesized intentionally. The coordination configuration of the synthesized catalyst ($FeCoN_x$/C) was researched by least-squares EXAFS fitting analysis. Actually, the M–N coordination number is less than 4, meaning that the configuration of $FeCoN_x$/C isn't a simple superposition of FeN_4 and CoN_4. Besides, there are particular Fe-X and Co-X paths (2.1–2.2 Å), which can be attributed to the Fe–Co contribution, and the Fe–Co bond length agrees well with the distance of two atoms observed from the AC-HAADF-STEM image (Fig. 15g). $FeCoN_x$/C reached an extraordinary $E_{1/2}$ of 0.86 V in 0.1 M $HClO_4$, and this performance exceeds the current state-of-the-art non-precious metal catalysts, which can be attributed to the extremely high intrinsic activity of the $FeCoN_5$–OH site. Chen *et al.*[113] then proposed the doping of Co atoms in the Fe–N–C catalyst (FeCo–NC-3), which not only boosts the catalytic activity, but also improves the stability of the catalysts. The HAADF-STEM and FT-EXAFS together proved the existence of Fe–Co binuclear sites, and the fitting Fe K-edge EXAFS confirmed that the coordination numbers of Fe–N and Co–N are both close to 4, so the most likely structure of active sites is shown in Fig. 15h. After testing, the $E_{1/2}$ of FeCo–NC-3 is 0.842 V in 0.1 M $HClO_4$ and the $E_{1/2}$ decreased by only 11 mV after 10 000 cycles. The reason for the improvement in catalytic performance is the introduction of Co atoms that increases the electron density of Fe center sites, which can be attested by experimental results of XPS and Fe Mössbauer spectroscopy; the results of Mössbauer spectroscopy are summarized in Fig. 15i. The D1, D2 and D3 respectively represent the signature active low-spin Fe^{II}–N_4 structure, inactive low-spin N–(Fe^{II}–N_4)–N structure and mid-spin FePc-like Fe^{II}–N_4 species. After introduction of Co, the content of inactive D2 is reduced while D1 is significantly increased, so the valence of Fe changes from +3 to +2, resulting in increased activity. A study demonstrated that two *OH adsorbing on the same side of Fe to form *$Fe(OH)_2$ will lead to Fe site leaching and subsequent performance degradation.[114] Inspired by experiments, the author used DFT calculation to prove the good stability of FeCo–NC-3. The reason is that *OH is difficult to adsorb stably on the $FeCoN_6$ site to form *$Fe(OH)_2$, thus avoiding damage of Fe sites.

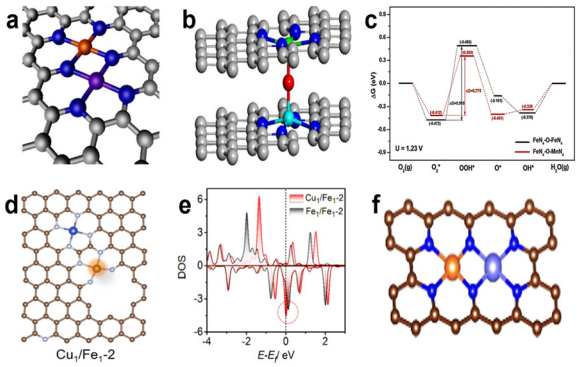

Fig. 16 (a) The structure of Fe,Mn/N_6.[115] (b) The model of active site FeN_4–O–MnN_4.[116] (c) The free energy evolution diagram on FeN_4–O–FeN_4 and FeN_4–O–MnN_4 sites for the ORR.[116] (d) The structure of NCAG/Fe–Cu near the nanopore edge.[117] (e) Fe 3d DOS of Fe_1/Fe_1-2 and Cu_1/Fe_1-2.[117] (f) The structure of $FeZnN_6$ moieties.[120]

4.2 Other dual-metals as active centers

Aside from the usual Fe–Co bimetals, other dual-metals as active centers were also researched. In recent years, researchers have discovered that the spin states of Fe are related to the catalytic activity and stability, which stimulated the research on the regulation of Fe spin states. Yang *et al.*[115] prepared a catalyst containing Fe–Mn dual-metal (Fe,Mn/N–C), the structure of the active site is shown in Fig. 16a, and the structure was verified by K-edge XANES and K-edge FT-EXAFS of Fe and Mn. This catalyst reached an $E_{1/2}$ of 0.804 V in 0.1 M $HClO_4$, and the good performance can be attributed to the single-atom dispersed Mn–N moieties effectively adjusting the electron configuration and spin states of Fe^{III} (from the low spin state to the ideal intermediate spin state), which allows the active sites to have a suitable adsorption strength with oxygen intermediates. Moreover, Cai *et al.*[116] synthesized a catalyst with FeN_4 and MnN_4 species, and FeN_4 and MnN_4 are linked together by an oxygen atom, forming a new active site (FeN_4–O–MnN_4), as shown in Fig. 16b. According to the fitting FT EXAFS, the coordination numbers of Fe–N/O and Mn–N/O are 4.6 and 5.1, respectively. Combined with O 1s XPS spectral results, the presence of the metal–O bond demonstrated the rationality of the structure of O as a bridge connecting FeN_4 and MnN_4. The catalyst exhibited an $E_{1/2}$ of 0.781 V, slightly lower than 20% Pt/C. The introduction of Mn can not only increase the content of Fe, but also reduce the energy barrier of the ORR (Fig. 16c). He and colleagues[117] then discovered that introduction of Cu can also regulate the spin-state of FeN_4, especially near the nanopore edge. The possible structure of NCAG/Fe–Cu is shown in Fig. 16d. DFT calculations show that the introduction of Cu can regulate the Fe 3d density of states (DOS), making the DOS closer to the Fermi energy level than without Cu (Fig. 16e), which can improve the catalytic

performance. Du *et al.*[118] and Song *et al.*[119] also synthesized catalysts which contain two metallic elements, Fe and Cu, and the structure of the active sites is mostly a simple combination of FeN_4 and CuN_4. These articles both proved that trace amounts of Cu atoms doped in the carbon matrix that is close to Fe can facilitate the formation of FeN_4 and promote the catalytic activity and stability. Aiming at solving the problem of the stability of M–N–C catalysts being affected by the destruction of the active site caused by the protonation of nitrogen, Li *et al.*[120] screened an Fe–Zn based bimetal catalyst with high stability through theoretical calculations. Fe and Zn K-edge EXAFS show a weak peak at 2.36 Å which demonstrated the interaction between Fe and Zn, and the fitting data proved the structure of $FeZnN_6$; the structure is shown in Fig. 16f (Fe/Zn–N–C). Fe/Zn–N–C reached an $E_{1/2}$ of 0.808 V, and the $E_{1/2}$ lost only 12 mV after 5000 potential cycles in 0.1 M $HClO_4$. The good performance of Fe/Zn–N–C can be attributed to the $FeZnN_6$ moieties showing high protonation free energy, and the breaking of the Zn–N bond to protect the active structure of FeN_4 during protonation.

In addition to the bimetallic-site catalysts mentioned above, bimetal site catalysts formed by Co and other metals have also been studied by many people. For example, Li and colleagues[121] prepared a catalyst which contained carbon-coated CoNi alloy and M–N_4 sites (Co_xNi–N/C). XRD patterns exhibit three identified peaks, which correspond to the (111), (200), and (220) lattice planes of metallic Ni and Co, respectively (Fig. 17a). However, the position of these peaks is offset from the standard position recorded in the database, which reflects the presence of CoNi alloys. High-resolution XPS spectra of Co 2p and Ni 2p demonstrated the coordination environment of Co–N_x and Ni–N_x. Experiments showed that introduction of Ni increased the amount of pyridine-N and Co–N moieties, and the interaction between CoNi alloys and M–N–C moieties can adjust the electron density of M–N–C moieties, facilitating the catalytic activity. Moreover, Zhang *et al.*[122] prepared a novel catalyst that encapsulated a thin Cu layer and Co nanoparticles in graphitic carbon layers, forming abundant M-NPs and M–N_x atomic sites. The electron-donating effect of M-NPs can regulate the electron density of M–N_x. DFT calculations show that about 0.05 e^- are transferred from a Cu slab to the CoN_4 sites. So, the interaction of Co and Cu enhances the ORR activity toward both H_2O and H_2O_2 (Fig. 17b). In addition, Shah *et al.*[123] produced porous N-doped carbon nanostructures with Mn-/Co–N_x dual moieties (MnCo–NC/CNT) which exhibited excellent catalytic activity and stability in acid environment. The high-resolution Mn 2p and Co 2p spectra demonstrated the presence of Co–N_x and Mn–N_x moieties, which act as the most important active sites to catalyze the ORR, as shown in Fig. 17c and d. The doping of Mn improved the selectivity of the four-electron ORR pathway of Co–N–C catalysts, and the H_2O_2 yield was less than 5% in acid medium. It can be seen that the synergistic effect of bimetallic sites can improve the performance of catalysts. In addition to experimental studies, the stability and activity of active sites can also be predicted by theoretical calculations. Wang *et al.*[124] systematically studied the intrinsic nature of the Zn–Co bimetallic catalyst in the oxygen reduction reaction by DFT calculations. In order to better understand the effect of the structure of the active site on the catalytic activity and stability, the authors simulated a variety of configurations, labeled as $ZnCoN_x$-gra (x = 1–6). Calculation results show that when $x < 4$, the structures are thermodynamically unstable, and the stability of the active site increases with the increase of x value. The most stable configuration is shown in Fig. 17e. Besides, this research discovered that the catalytic activity of the ORR was enhanced when the active sites were combined with electron-withdrawing functional groups, especially with two *OH (Fig. 17f). The conclusion is consistent with the research of Cao *et al.*[125] And Zn tends to sacrifice itself to protect the Co active center during the catalytic reaction, which is conducive to stabilization.

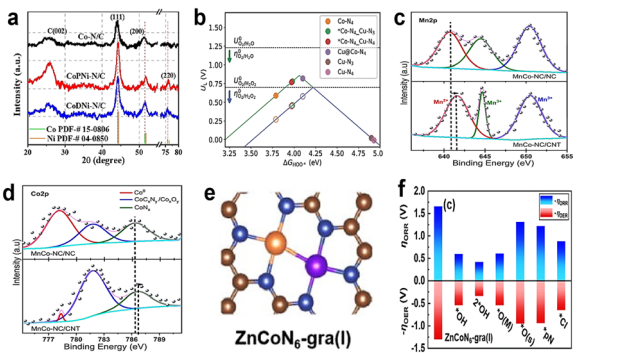

Fig. 17 (a) XRD patterns of Co–N/C, CoXNi–N/C (X = P and D).[121] (b) The volcano plots for the four-electron ORR to H_2O (solid circles) and two-electron ORR to H_2O_2 (empty circles).[122] High-resolution (c) Mn 2p and (d) Co 2p spectra of MnCo–NC/NC and MnCo–NC/CNT.[123] (e) The most stable configuration of $ZnCoN_x$-gra.[124] (f) The overpotential of the ORR and OER for $ZnCoN_6$-gra (I) with or without electron-withdrawing functional groups.[124]

5 Conclusions and outlook

Developing low-cost and high-efficiency PGM-free ORR catalysts in acidic media is important for application of PEMFCs. After decades of development, the performance of catalysts has been greatly improved. However, we also need to clearly recognize that the catalysts currently studied are not enough to be used in practical production, especially in acidic environment, and there is still a big gap between their performance and state-of-the-art Pt/C. Therefore, how to effectively improve the catalytic activity and stability of non-noble metals is still a hot research issue. Next, we will summarize the challenges and some common strategies for improving the activity and stability of non-noble metal oxygen reduction catalysts.

As one of the important parameters for evaluating oxygen reduction catalysts, the half-wave potential can initially determine the activity of catalysts. However, the activity of

most non-precious metals in the three-electrode test is about 50 mV lower than that of commercial Pt/C, which is mainly due to (1) the low intrinsic activity of non-precious metals. As shown in Fig. 3a, compared with other non-precious metals, Pt is closer to the peak of the volcanic curve, which means that Pt has appropriate adsorption energy for the intermediate of the oxygen reduction reaction, and therefore presents the best activity, while most transition metals such as Fe and Co often show weak reactivity due to their strong adsorption. (2) Insufficient density of active sites. Since Zhang *et al.* proposed SACs,[49] people began to study single-atom oxygen reduction catalysts extensively and proved their superiority. But SACs often mean low metal content, because increasing the metal content causes the metal atoms to gather together and become less active.[84,126] Therefore, monatomic catalysts with high intrinsic activity face the problem of insufficient active sites. (3) Insufficient exposure of active sites. At present, most catalysts use a metal organic frame and other materials with fence function to restrict metal aggregation and form monatomic catalysts. The typical precursor is ZIF-8, but the catalyst formed by this is mainly composed of micropores, which hinders the diffusion of O_2 and makes it difficult for O_2 to approach the active site, thus reducing the utilization rate of the active site.[67] These reasons all lead to insufficient activity expression of non-precious metals. Understanding these reasons can help us design catalysts reasonably. The following are some common strategies for improving catalyst activity:

The improvement in catalytic activity is mainly achieved *via* the following techniques: (1) increasing the density of active sites. Many studies have proved that the number of active sites is positively correlated with catalytic activity. Increasing the active site density means increasing the number of species reacting per unit time, simultaneously increasing the reaction rate. (2) Designing catalysts with high-intrinsic activity. In order to achieve this goal, it's necessary to define the main active site and determine the main factors affecting the performance. The completion of these steps can't be separated from the guidance of theoretical calculations. With the development of computer technology, using DFT to design the catalyst has a good guiding significance. (3) Improving the utilization rate of the active center. In recent years, the development of single-atom site catalysts has efficiently improved the utilization rate, but a major problem of such catalysts is the low metal loading, which leads to a low density of active sites. Therefore, efforts should be made in the future to increase the number of single atomic metal sites as much as possible without causing metal aggregation. (4) Increasing the exposure of active sites. The catalytic activity of metal sites covered by carbon layers is lower than that of sites exposed to carbon layers. The hierarchical porous structure of the catalyst is favorable for exposing more active sites and increases the mass transfer rates of reactants and products.

Now, it's found that the main reasons for the poor stability of catalytic include: (1) demetallization of the active site. (2) H_2O_2 or hydroperoxyl radical oxidative species attack. (3) Corrosion of carbon substrates. (4) Micropore flooding. According to the previous introduction, Fe has been widely studied as a non-noble metal with the highest oxygen reduction reactivity. However, current studies have shown that Fe has strong Fenton activity and reacts with H_2O_2 to form highly active oxygen-containing radicals during the reaction. These free radicals attack the active center and carbon substrate of the catalyst, resulting in demetallization and carbon corrosion of the catalyst. This is the main factor contributing to the inactivation of the catalyst. In addition, because the product of the oxygen reduction reaction is water, and the active site is concentrated in the micropores, it is difficult for the product water to be discharged in time, resulting in the active site being buried, thus resulting in a decrease in catalyst activity. Some strategies have made great progress in improving stability, such as incorporation of activated biomasses in catalysts to enhance stability,[127] improving the graphitization degree of the carbon substrate[128] and so on. There are several ways to improve the stability of catalysts by changing the active site: (1) change the electronic structure near the active site to improve the M–N bond strength. (2) Look for alternative metals to Fe. According to the reasons for the decline in catalyst performance described above, we can replace Fe with non-precious metals with weak Fenton activity or even no Fenton activity, such as Co, Mn, *etc.* to improve the stability of the catalyst. (3) Exploring suitable dual-metal catalysts. The synergistic effect between bimetals can effectively regulate the electronic structure around the active sites, thus affecting the stability of the catalysts.[3] (4) Construction of catalysts with micro–meso-composite pore structures. Materials with rich mesopores are selected as carbon substrates to promote the transport of substances in the reaction process and reduce the harm caused by micropore flooding.

At present, the methods for preparing high-performance ORR non-noble metal catalysts can be summarized as the template method, chemical vapor deposition method, heteroatom modification method, *etc.* (1) Template method. By adding an additional substance as a template to limit the shape and size of the carbon substrate, a carbon substrate with a porous structure can be obtained by removing the template in a subsequent step. Using its porous structure, the active site density of the catalyst can be increased, thus improving the activity of the catalyst. For example, Wan *et al.* used SiO_2 as a template to construct ZIF-8 with a concave surface through high-temperature pyrolysis and subsequent steps to remove the template, thereby forming a single-atom Fe–N–C catalyst with high active site density, and its Fe content can reach 3 wt%.[129] In addition, because the catalyst is concave, its external surface area is large, which also promotes the exposure of the active site. Experiments show that the template method is an effective method for constructing high-performance catalysts, but this method usually faces the dilemma that the template is difficult to remove. In addition, there are reports of using molten salts

such as KCl and NaCl as templates; using the melting characteristics of the molten salt under high temperature conditions, the molten salt can be removed by simple washing to form a porous carbon substrate. For example, Wang *et al.* used NaCl as a template, NaCl melted and coated on the surface of ZIF-8 under high temperature conditions, and a N-containing carbon substrate with a porous structure could be obtained after NaCl was removed by subsequent water washing.[130] Similarly, this method increases the active site density and effectively improves the performance of the catalyst. (2) Chemical vapor deposition (CVD) method. Chemical vapor deposition refers to the reaction of chemical gases or vapors on the substrate surface to synthesize coatings or nanomaterials. A typical example of the chemical vapor deposition method is when Jiao *et al.* used anhydrous $FeCl_3$ as an iron source and ZIF-8 as a C source containing N. $FeCl_3$ was adsorbed on ZIF-8 by the method of CVD. Under the condition of high temperature, Fe and Zn exchanged to form Fe–N_4 sites with high activity. In addition, because Fe is mostly located on the surface of the catalyst, the active site utilization rate of the catalyst is extremely high, reaching 100%.[131] Although this method has not been studied much in the preparation of ORR non-precious metal catalysts, according to the high-performance catalyst prepared by this method, the CVD method will be a potential method to be further explored. (3) Heteroatom modification method. Heteroatom doping is usually the doping of atoms such as P, S, B and F into the N-containing carbon substrate through high-temperature pyrolysis to regulate the electron density near the active site, so as to achieve the purpose of improving the activity of the catalyst. Although these methods can improve the performance of catalysts to a certain extent, there are still some problems in the preparation of non-noble metal oxygen reduction catalysts, such as the high temperature pyrolysis method takes a long time, the catalyst is difficult to be prepared in batch, and the organic matter used in the preparation process causes great pollution to the environment. These problems have seriously hindered the commercial application of ORR non-precious metal catalysts. Therefore, the development of other efficient and clean preparation methods is the direction of our future efforts.

In summary, improving the performance of ORR catalyst is of great significance to the wide application of PEMFCs. In fact, the structure of the catalyst active site is closely related to the performance of the catalyst, so it is necessary to determine the structure of the active site through advanced characterization techniques and reasonable simulation calculations in the study of catalysts. The application process of PEMFCs can be effectively accelerated by combining theoretical calculation with experimental techniques to design and manufacture efficient catalysts.

Conflicts of interest

The authors declare no conflict of interest.

Acknowledgements

The authors would like to thank the National Key R&D Program (2022YFB4004100), National Natural Science Foundation of China (21875243, 21673221, 22209168), Jilin Province Science and Technology Development Program (20200201001JC, 20190201270JC, 20180101030JC) and Special Funds for Guiding Local Scientific, Technological Development by the Central Government (Grant No. 2020JH6/10500021).

References

1 J. Lian, J. Y. Zhao and X. M. Wang, Recent Progress in Carbon-based Materials of Non-Noble Metal Catalysts for ORR in Acidic Environment, *Acta Metall. Sin.*, 2021, **34**, 885–899.
2 K. Song, Y. Feng, W. Zhang and W. Zheng, MOFs fertilized transition-metallic single-atom electrocatalysts for highly-efficient oxygen reduction: Spreading the synthesis strategies and advanced identification, *J. Energy Chem.*, 2022, **67**, 391–422.
3 Y. H. He, S. W. Liu, C. Priest, Q. R. Shi and G. Wu, Atomically dispersed metal-nitrogen-carbon catalysts for fuel cells: advances in catalyst design, electrode performance, and durability improvement, *Chem. Soc. Rev.*, 2020, **49**, 3484–3524.
4 R. Jasinski, New fuel cell cathode catalyst, *Nature*, 1964, **201**, 1212–1213.
5 S. Liu, Z. Li, C. Wang, W. Tao, M. Huang, M. Zuo, Y. Yang, K. Yang, L. Zhang, S. Chen, P. Xu and Q. Chen, Turning main-group element magnesium into a highly active electrocatalyst for oxygen reduction reaction, *Nat. Commun.*, 2020, **11**, 938.
6 T. Iida, M. Shetty, K. Murugappan, Z. Wang, K. Ohara, T. Wakihara and Y. Roman-Leshkov, Encapsulation of Molybdenum Carbide Nanoclusters inside Zeolite Micropores Enables Synergistic Bifunctional Catalysis for Anisole Hydrodeoxygenation, *ACS Catal.*, 2017, **7**, 8147–8151.
7 M. Xiao, J. Zhu, L. Feng, C. Liu and W. Xing, Meso/Macroporous Nitrogen-Doped Carbon Architectures with Iron Carbide Encapsulated in Graphitic Layers as an Efficient and Robust Catalyst for the Oxygen Reduction Reaction in Both Acidic and Alkaline Solutions, *Adv. Mater.*, 2015, **27**, 2521–2527.
8 T. Patniboon and H. A. Hansen, Acid-Stable and Active M–N–C Catalysts for the Oxygen Reduction Reaction: The Role of Local Structure, *ACS Catal.*, 2021, **11**, 13102–13118.
9 H. Yang, X. Chen, W. T. Chen, Q. Wang, N. C. Cuello, A. Nafady, A. M. Al-Enizi, G. I. N. Waterhouse, G. A. Goenaga, T. A. Zawodzinski, P. E. Kruger, J. E. Clements, J. Zhang, H. Tian, S. G. Telfer and S. Ma, Tunable Synthesis of Hollow Metal-Nitrogen-Carbon Capsules for Efficient Oxygen Reduction Catalysis in Proton Exchange Membrane Fuel Cells, *ACS Nano*, 2019, **13**, 8087–8098.

10 N. Behera, S. P. Mantry, B. D. Mohapatra, R. K. Behera and K. S. K. Varadwaj, Functional molecule guided evolution of MnOx nanostructure patterns on N-graphene and their oxygen reduction activity, *RSC Adv.*, 2019, **9**, 27945–27952.

11 J. Liu, L. Jiang, B. Zhang, J. Jin, D. S. Su, S. Wang and G. Sun, Controllable Synthesis of Cobalt Monoxide Nanoparticles and the Size-Dependent Activity for Oxygen Reduction Reaction, *ACS Catal.*, 2014, **4**, 2998–3001.

12 J. Xu, P. Gao and T. S. Zhao, Non-precious Co3O4 nano-rod electrocatalyst for oxygenreduction reaction in anion-exchange membranefuelcells, *Energy Environ. Sci.*, 2012, **5**, 5333–5339.

13 K. P. Singh, E. J. Bae and J. S. Yu, Fe-P: a new class of electroactive catalyst for oxygen reduction reaction, *J. Am. Chem. Soc.*, 2015, **137**, 3165–3168.

14 Z. Miao, X. Wang, Z. Zhao, W. Zuo, S. Chen, Z. Li, Y. He, J. Liang, F. Ma, H. L. Wang, G. Lu, Y. Huang, G. Wu and Q. Li, Improving the Stability of Non-Noble-Metal M-N-C Catalysts for Proton-Exchange-Membrane Fuel Cells through M-N Bond Length and Coordination Regulation, *Adv. Mater.*, 2021, **33**, e2006613.

15 M. Xiao, Y. Chen, J. Zhu, H. Zhang, X. Zhao, L. Gao, X. Wang, J. Zhao, J. Ge, Z. Jiang, S. Chen, C. Liu and W. Xing, Climbing the Apex of the ORR Volcano Plot via Binuclear Site Construction: Electronic and Geometric Engineering, *J. Am. Chem. Soc.*, 2019, **141**, 17763–17770.

16 J. Prakash, D. A. Tryk and E. B. Yeager, Kinetic investigations of oxygen reduction and evolution reactions on lead ruthenate catalysts, *J. Electrochem. Soc.*, 1999, **146**, 4145–4151.

17 T. Sun, S. Mitchell, J. Li, P. Lyu, X. Wu, J. Perez-Ramirez and J. Lu, Design of Local Atomic Environments in Single-Atom Electrocatalysts for Renewable Energy Conversions, *Adv. Mater.*, 2021, **33**, e2003075.

18 F. Liu, L. Shi, X. Lin, D. Yu, C. Zhang, R. Xu, D. Liu, J. Qiu and L. Dai, Site-density engineering of single-atomic iron catalysts for high-performance proton exchange membrane fuel cells, *Appl. Catal., B*, 2022, **302**, 120860–120871.

19 Y. Yan, H. Y. Cheng, Z. H. Qu, R. Yu, F. Liu, Q. W. Ma, S. Zhao, H. Hu, Y. Cheng, C. Y. Yang, Z. F. Li, X. Wang, S. Y. Hao, Y. Y. Chen and M. K. Liu, Recent progress on the synthesis and oxygen reduction applications of Fe-based single-atom and double-atom catalysts, *J. Mater. Chem. A*, 2021, **9**, 19489–19507.

20 W. Zou, R. Lu, X. Liu, G. Xiao, X. Liao, Z. Wang and Y. Zhao, Theoretical insights into dual-atom catalysts for the oxygen reduction reaction: the crucial role of orbital polarization, *J. Mater. Chem. A*, 2022, **10**, 9150–9160.

21 J. Wang, C. X. Zhao, J. N. Liu, Y. W. Song, J. Q. Huang and B. Q. Li, Dual-atom catalysts for oxygen electrocatalysis, *Nano Energy*, 2022, **104**, 107927–107940.

22 V. Stamenkovic, B. S. Mun, K. J. Mayrhofer, P. N. Ross, N. M. Markovic, J. Rossmeisl, J. Greeley and J. K. Norskov, Changing the activity of electrocatalysts for oxygen reduction by tuning the surface electronic structure, *Angew. Chem., Int. Ed.*, 2006, **45**, 2897–2901.

23 J. K. Norskov, J. Rossmeisl, A. Logadottir, L. Lindqvist, J. R. Kitchin, T. Bligaard and H. Jonsson, Origin of the overpotential for oxygen reduction at a fuel-cell cathode, *J. Phys. Chem. B*, 2004, **108**, 17886–17892.

24 H. Xu, D. Cheng, D. Cao and X. C. Zeng, A universal principle for a rational design of single-atom electrocatalysts, *Nat. Catal.*, 2018, **1**, 339–348.

25 D. Deng, L. Yu, X. Chen, G. Wang, L. Jin, X. Pan, J. Deng, G. Sun and X. Bao, Iron encapsulated within pod-like carbon nanotubes for oxygen reduction reaction, *Angew. Chem., Int. Ed.*, 2013, **52**, 371–375.

26 M. Xiao, J. Zhu, C. Liu, J. Ge and W. Xing, Recent Progress in Non-Precious Metal Oxygen Reduction Reaction Catalysts with an Encapsulation Structure, *J. Electrochem.*, 2016, **22**, 101–112.

27 D. Guo, R. Shibuya, C. Akiba, S. Saji, T. Kondo and J. Nakamura, Active sites of nitrogen-doped carbon materials for oxygen reduction reaction clarified using model catalysts, *Science*, 2016, **351**, 361–365.

28 Y. Jia, L. Zhang, L. Zhuang, H. Liu, X. Yan, X. Wang, J. Liu, J. Wang, Y. Zheng, Z. Xiao, E. Taran, J. Chen, D. Yang, Z. Zhu, S. Wang, L. Dai and X. Yao, Identification of active sites for acidic oxygen reduction on carbon catalysts with and without nitrogen doping, *Nat. Catal.*, 2019, **2**, 688–695.

29 T. Sun, Y. Jiang, Q. Wu, L. Du, Z. Zhang, L. Yang, X. Wang and Z. Hu, Is iron nitride or carbide highly active for oxygen reduction reaction in acidic medium?, *Catal. Sci. Technol.*, 2017, **7**, 51–55.

30 C. Zhu, H. Li, S. Fu, D. Du and Y. Lin, Highly efficient nonprecious metal catalysts towards oxygen reduction reaction based on three-dimensional porous carbon nanostructures, *Chem. Soc. Rev.*, 2016, **45**, 517–531.

31 J. Masa, W. Xia, M. Muhler and W. Schuhmann, On the Role of Metals in Nitrogen-Doped Carbon Electrocatalysts for Oxygen Reduction, *Angew. Chem., Int. Ed.*, 2015, **54**, 10102–10120.

32 Z. Chen, D. Higgins, A. Yu, L. Zhang and J. Zhang, A review on non-precious metal electrocatalysts for PEM fuel cells, *Energy Environ. Sci.*, 2011, **4**, 3167–3192.

33 X. L. Tian, X. F. Lu, B. Y. Xia and X. W. Lou, Advanced Electrocatalysts for the Oxygen Reduction Reaction in Energy Conversion Technologies, *Joule*, 2020, **4**, 45–68.

34 S. Gupta, D. Tryk, I. Bae, W. Aldred and E. Yeager, Heat-treated polyacrylonitrile-based catalysts for oxygen electroreduction, *J. Appl. Electrochem.*, 1989, **19**, 19–27.

35 U. Martinez, S. Komini Babu, E. F. Holby, H. T. Chung, X. Yin and P. Zelenay, Progress in the Development of Fe-Based PGM-Free Electrocatalysts for the Oxygen Reduction Reaction, *Adv. Mater.*, 2019, **31**, e1806545.

36 M. Lefevre, J. P. Dodelet and P. Bertrand, Molecular oxygen reduction in PEM fuel cells: Evidence for the simultaneous presence of two active sites in Fe-based catalysts, *J. Phys. Chem. B*, 2002, **106**, 8705–8713.

37 Y. Li, X. Liu, L. Zheng, J. Shang, X. Wan, R. Hu, X. Guo, S. Hong and J. Shui, Preparation of Fe–N–C catalysts with FeNx (x = 1, 3, 4) active sites and comparison of their

activities for the oxygen reduction reaction and performances in proton exchange membrane fuel cells, *J. Mater. Chem. A*, 2019, **7**, 26147–26153.

38 L. Liu, X. Yang, N. Ma, H. Liu, Y. Xia, C. Chen, D. Yang and X. Yao, Scalable and Cost-Effective Synthesis of Highly Efficient Fe2N-Based Oxygen Reduction Catalyst Derived from Seaweed Biomass, *Small*, 2016, **12**, 1295–1301.

39 H. M. Fruehwald, I. I. Ebralidze, O. V. Zenkina and E. B. Easton, Fe-N-3/C Active Catalytic Sites for the Oxygen Reduction Reaction Prepared with Molecular-Level Geometry Control through the Covalent Immobilization of an Iron-Terpyridine Motif onto Carbon, *ChemElectroChem*, 2019, **6**, 1350–1358.

40 X. Qin, S. Zhu, L. Zhang, S. Sun and M. Shao, Theoretical Studies of Metal-N-C for Oxygen Reduction and Hydrogen Evolution Reactions in Acid and Alkaline Solutions, *J. Electrochem.*, 2021, **27**, 185–194.

41 G. Wu and P. Zelenay, Nanostructured Nonprecious Metal Catalysts for Oxygen Reduction Reaction, *Acc. Chem. Res.*, 2013, **46**, 1878–1889.

42 E. Proietti, F. Jaouen, M. Lefevre, N. Larouche, J. Tian, J. Herranz and J. P. Dodelet, Iron-based cathode catalyst with enhanced power density in polymer electrolyte membrane fuel cells, *Nat. Commun.*, 2011, **2**, 416–424.

43 D. Liu, G. Goenaga, S. Ma, S. Yuan and J. Shui, New Approaches to Non-PGM Catalysts through Rational Design, *ECS Trans.*, 2011, **30**, 97–104.

44 X. Wang, H. Zhang, H. Lin, S. Gupta, C. Wang, Z. Tao, H. Fu, T. Wang, J. Zheng, G. Wu and X. Li, Directly converting Fe-doped metal–organic frameworks into highly active and stable Fe-N-C catalysts for oxygen reduction in acid, *Nano Energy*, 2016, **25**, 110–119.

45 M. Xu, J. Liu, J. Ge, C. Liu and W. Xing, Research Progress of Metal-Nitrogen-Carbon Catalysts toward Oxygen Reduction Reaction in Changchun Institute of Applied Chemistry, *Dianhuaxue*, 2020, **26**, 464–473.

46 J. G. Speight, *Lange's handbook of chemistry*, McGraw-hill New York, 2005.

47 S. Poulin, R. Franca, L. Moreau-Belanger and E. Sacher, Confirmation of X-ray Photoelectron Spectroscopy Peak Attributions of Nanoparticulate Iron Oxides, Using Symmetric Peak Component Line Shapes, *J. Phys. Chem. C*, 2010, **114**, 10711–10718.

48 T. Yamashita and P. Hayes, Analysis of XPS spectra of Fe2+ and Fe3+ ions in oxide materials, *Appl. Surf. Sci.*, 2008, **254**, 2441–2449.

49 B. Qiao, A. Wang, X. Yang, L. F. Allard, Z. Jiang, Y. Cui, J. Liu, J. Li and T. Zhang, Single-atom catalysis of CO oxidation using Pt-1/FeOx, *Nat. Chem.*, 2011, **3**, 634–641.

50 Q. Qu, S. Ji, Y. Chen, D. Wang and Y. Li, Design and structural engineering of single-atomic-site catalysts for acidic oxygen reduction reaction, *Trends Chem.*, 2021, **3**, 954–968.

51 Q. Ren, H. Wang, X. F. Lu, Y. X. Tong and G. R. Li, Recent Progress on MOF-Derived Heteroatom-Doped Carbon-Based Electrocatalysts for Oxygen Reduction Reaction, *Adv. Sci.*, 2018, **5**, 1700515.

52 L. Deng, L. Qiu, R. Hu, L. Yao, Z. Zheng, X. Ren, Y. Li and C. He, Restricted diffusion preparation of fully-exposed Fe single-atom catalyst on carbon nanospheres for efficient oxygen reduction reaction, *Appl. Catal., B*, 2022, **305**, 121058–121067.

53 H. Xu, D. Wang, P. Yang, L. Du, X. Lu, R. Li, L. Liu, J. Zhang and M. An, A hierarchically porous Fe-N-C synthesized by dual melt-salt-mediated template as advanced electrocatalyst for efficient oxygen reduction in zinc-air battery, *Appl. Catal., B*, 2022, **305**, 121040–121051.

54 X. Wang, C. Yang, X. Wang, H. Zhu, L. Cao, A. Chen, L. Gu, Q. Zhang, L. Zheng and H.-P. Liang, Green Synthesis of a Highly Efficient and Stable Single-Atom Iron Catalyst Anchored on Nitrogen-Doped Carbon Nanorods for the Oxygen Reduction Reaction, *ACS Sustainable Chem. Eng.*, 2020, **9**, 137–146.

55 L. Li, Y. Wen, G. Han, Y. Liu, Y. Song, W. Zhang, J. Sun, L. Du, F. Kong, Y. Ma, Y. Gao, J. Wang, C. Du and G. Yin, Tailoring the stability of Fe-N-C via pyridinic nitrogen for acid oxygen reduction reaction, *Chem. Eng. J.*, 2022, **437**, 135320–135327.

56 X. Xiang, X. Zhang, B. Yan, K. Wang, Y. Wang, D. Lyu, S. Xi, Z. Qun Tian and P. Kang Shen, Atomic iron coordinated by nitrogen doped carbon nanoparticles synthesized via a synchronous complexation-polymerization strategy as efficient oxygen reduction reaction electrocatalysts for zinc-air battery and fuel cell application, *Chem. Eng. J.*, 2022, **440**, 135721–135733.

57 W. J. Jiang, L. Gu, L. Li, Y. Zhang, X. Zhang, L. J. Zhang, J. Q. Wang, J. S. Hu, Z. Wei and L. J. Wan, Understanding the High Activity of Fe-N-C Electrocatalysts in Oxygen Reduction: Fe/Fe3C Nanoparticles Boost the Activity of Fe-N(x), *J. Am. Chem. Soc.*, 2016, **138**, 3570–3578.

58 S. Zhang, M. Chen, X. Zhao, J. Cai, W. Yan, J. C. Yen, S. Chen, Y. Yu and J. Zhang, Advanced Noncarbon Materials as Catalyst Supports and Non-noble Electrocatalysts for Fuel Cells and Metal–Air Batteries, *Electrochem. Energy Rev.*, 2021, **4**, 336–381.

59 M. Wang, T. Liao, X. Zhang, J. Cao, S. Xu, H. Tang and Y. Wang, Electrospun Carbon Nanofibers Loaded with Atomic FeNx/Fe2O3 Active Sites for Efficient Oxygen Reduction Reaction in Both Acidic and Alkaline Media, *Adv. Mater. Interfaces*, 2022, **9**, 2101904–2101914.

60 C. Xu, L. Chen, Y. Wen, S. Qin, H. Li, Z. Hou, Z. Huang, H. Zhou and Y. Kuang, A co-operative protection strategy to synthesize highly active and durable Fe/N co–doped carbon towards oxygen reduction reaction in Zn–air batteries, *Mater. Today Energy*, 2021, **21**, 100721–100731.

61 Z. Xu, J. Ma, M. Shi, Y. Xie and C. Feng, Biomass based iron and nitrogen co-doped 3D porous carbon as an efficient oxygen reduction catalyst, *J. Colloid Interface Sci.*, 2018, **523**, 144–150.

62 X. Liu, H. Liu, C. Chen, L. Zou, Y. Li, Q. Zhang, B. Yang, Z. Zou and H. Yang, Fe2N nanoparticles boosting FeNx moieties for highly efficient oxygen reduction reaction in Fe-N-C porous catalyst, *Nano Res.*, 2019, **12**, 1651–1657.

63 S. Liu, Q. Meyer, Y. Li, T. Zhao, Z. Su, K. Ching and C. Zhao, Fe–N–C/Fe nanoparticle composite catalysts for the oxygen reduction reaction in proton exchange membrane fuel cells, *Chem. Commun.*, 2022, **58**, 2323–2326.

64 M. X. Chen, M. Zhu, M. Zuo, S. Q. Chu, J. Zhang, Y. Wu, H. W. Liang and X. Feng, Identification of Catalytic Sites for Oxygen Reduction in Metal/Nitrogen-Doped Carbons with Encapsulated Metal Nanoparticles, *Angew. Chem., Int. Ed.*, 2020, **59**, 1627–1633.

65 H.-A. Chen, C.-L. Hsin, Y.-T. Huang, M. L. Tang, S. Dhuey, S. Cabrini, W.-W. Wu and S. R. Leone, Measurement of Interlayer Screening Length of Layered Graphene by Plasmonic Nanostructure Resonances, *J. Phys. Chem. C*, 2013, **117**, 22211–22217.

66 D. H. Deng, L. Yu, X. Q. Chen, G. X. Wang, L. Jin, X. L. Pan, J. Deng, G. Q. Sun and X. H. Bao, Iron Encapsulated within Pod-like Carbon Nanotubes for Oxygen Reduction Reaction, *Angew. Chem., Int. Ed.*, 2013, **52**, 371–375.

67 C.-W. Ye and L. Xu, Recent advances in the design of a high performance metal–nitrogen–carbon catalyst for the oxygen reduction reaction, *J. Mater. Chem. A*, 2021, **9**, 22218–22247.

68 H. Li, K. Du, C. Xiang, P. An, X. Shu, Y. Dang, C. Wu, J. Wang, W. Du, J. Zhang, S. Li, H. Tian, S. Wang and H. Xia, Controlled chelation between tannic acid and Fe precursors to obtain N, S co-doped carbon with high density Fe-single atom-nanoclusters for highly efficient oxygen reduction reaction in Zn–air batteries, *J. Mater. Chem. A*, 2020, **8**, 17136–17149.

69 Y. Y. Meng, D. Voiry, A. Goswami, X. X. Zou, X. X. Huang, M. Chhowalla, Z. W. Liu and T. Asefa, N-, O-, and S-Tridoped Nanoporous Carbons as Selective Catalysts for Oxygen Reduction and Alcohol Oxidation Reactions, *J. Am. Chem. Soc.*, 2014, **136**, 13554–13557.

70 J. B. Zhu, K. Li, M. L. Xiao, C. P. Liu, Z. J. Wu, J. J. Ge and W. Xing, Significantly enhanced oxygen reduction reaction performance of N-doped carbon by heterogeneous sulfur incorporation: synergistic effect between the two dopants in metal-free catalysts, *J. Mater. Chem. A*, 2016, **4**, 7422–7429.

71 X. Hu, Y. Wu, H. Li and Z. Zhang, Adsorption and activation of O_2 on nitrogen-doped carbon nanotubes, *J. Phys. Chem. C*, 2010, **114**, 9603–9607.

72 L. Zhang, J. Niu, M. Li and Z. Xia, Catalytic mechanisms of sulfur-doped graphene as efficient oxygen reduction reaction catalysts for fuel cells, *J. Phys. Chem. C*, 2014, **118**, 3545–3553.

73 C. X. Zhao, B. Q. Li, J. N. Liu and Q. Zhang, Intrinsic Electrocatalytic Activity Regulation of M-N-C Single-Atom Catalysts for the Oxygen Reduction Reaction, *Angew. Chem., Int. Ed.*, 2021, **60**, 4448–4463.

74 H. Yin, P. Yuan, B.-A. Lu, H. Xia, K. Guo, G. Yang, G. Qu, D. Xue, Y. Hu, J. Cheng, S. Mu and J.-N. Zhang, Phosphorus-Driven Electron Delocalization on Edge-Type FeN4 Active Sites for Oxygen Reduction in Acid Medium, *ACS Catal.*, 2021, **11**, 12754–12762.

75 X. Liu, X. Zhai, W. Sheng, J. Tu, Z. Zhao, Y. Shi, C. Xu, G. Ge and X. Jia, Isolated single iron atoms anchored on a N, S-codoped hierarchically ordered porous carbon framework for highly efficient oxygen reduction, *J. Mater. Chem. A*, 2021, **9**, 10110–10119.

76 F. Xiao, G.-L. Xu, C.-J. Sun, M. Xu, W. Wen, Q. Wang, M. Gu, S. Zhu, Y. Li, Z. Wei, X. Pan, J. Wang, K. Amine and M. Shao, Nitrogen-coordinated single iron atom catalysts derived from metal organic frameworks for oxygen reduction reaction, *Nano Energy*, 2019, **61**, 60–68.

77 X. Tao, R. Lu, L. Ni, V. Gridin, S. H. Al-Hilfi, Z. Qiu, Y. Zhao, U. I. Kramm, Y. Zhou and K. Mullen, Facilitating the acidic oxygen reduction of Fe-N-C catalysts by fluorine-doping, *Mater. Horiz.*, 2022, **9**, 417–424.

78 M. Fan, Q. Yuan, Y. Zhao, Z. Wang, A. Wang, Y. Liu, K. Sun, J. Wu, L. Wang and J. Jiang, A Facile "Double-Catalysts" Approach to Directionally Fabricate Pyridinic NB-Pair-Doped Crystal Graphene Nanoribbons/Amorphous Carbon Hybrid Electrocatalysts for Efficient Oxygen Reduction Reaction, *Adv. Mater.*, 2022, **34**, e2107040.

79 K. Hu, L. Tao, D. Liu, J. Huo and S. Wang, Sulfur-Doped Fe/N/C Nanosheets as Highly Efficient Electrocatalysts for Oxygen Reduction Reaction, *ACS Appl. Mater. Interfaces*, 2016, **8**, 19379–19385.

80 J. Yan, Y. Liu, R. Wang, M. Xia, J. Wang, F. Gao and Y. Tang, Bamboo-like carbonitride nanotubes with multi-type active sites for oxygen reduction reaction in both alkaline and acid mediums, *Int. J. Hydrogen Energy*, 2022, **47**, 7949–7960.

81 H. Cheng, J.-M. Chen, Q.-J. Li, C.-Y. Su, A.-N. Chen, J.-X. Zhang, Z.-Q. Liu and Y. Tong, Modified molecular framework derived highly efficient Mn-Co-carbon cathode for a flexible Zn-air battery, *Chem. Commun.*, 2017, **53**, 11596–11599.

82 Z. Wang, S. Peng, Y. Hu, L. Li, T. Yan, G. Yang, D. Ji, M. Srinivasan, Z. Pan and S. Ramakrishna, Cobalt nanoparticles encapsulated in carbon nanotube-grafted nitrogen and sulfur co-doped multichannel carbon fibers as efficient bifunctional oxygen electrocatalysts, *J. Mater. Chem. A*, 2017, **5**, 4949–4961.

83 S. K. Mishra and S. B. Kanungo, Thermal Dehydeation and Decomposition of Cobalt Chloride Hydrate (CoCl2·xH2O), *J. Therm. Anal.*, 1992, **38**, 2437–2454.

84 Y. He, S. Hwang, D. A. Cullen, M. A. Uddin, L. Langhorst, B. Li, S. Karakalos, A. J. Kropf, E. C. Wegener, J. Sokolowski, M. Chen, D. Myers, D. Su, K. L. More, G. Wang, S. Litster and G. Wu, Highly active atomically dispersed CoN4 fuel cell cathode catalysts derived from surfactant-assisted MOFs: carbon-shell confinement strategy, *Energy Environ. Sci.*, 2019, **12**, 250–260.

85 G. Yang, F. Li, L. Wang, K. H. Row, H. Liu, L. Bai, W. Cao and T. Zhu, Synthesis, characteristics and evaluation of a new monolithic silica column prepared from copolymer pluronic F127, *Chromatographia*, 2008, **68**, 27–31.

86 J. Zhao, Y. Wang, W. Dong, Y. Wu, D. Li, B. Liu and Q. Zhang, A new surfactant-introduction strategy for separating the pure single-phase of metal-organic frameworks, *Chem. Commun.*, 2015, **51**, 9479–9482.

87 Y. He, H. Guo, S. Hwang, X. Yang, Z. He, J. Braaten, S. Karakalos, W. Shan, M. Wang, H. Zhou, Z. Feng, K. L. More, G. Wang, D. Su, D. A. Cullen, L. Fei, S. Litster and G. Wu, Single Cobalt Sites Dispersed in Hierarchically Porous Nanofiber Networks for Durable and High-Power PGM-Free Cathodes in Fuel Cells, *Adv. Mater.*, 2020, **32**, e2003577.

88 Z. Miao, Y. Xia, J. Liang, L. Xie, S. Chen, S. Li, H. L. Wang, S. Hu, J. Han and Q. Li, Constructing Co-N-C Catalyst via a Double Crosslinking Hydrogel Strategy for Enhanced Oxygen Reduction Catalysis in Fuel Cells, *Small*, 2021, **17**, e2100735.

89 M. Xiao, H. Zhang, Y. Chen, J. Zhu, L. Gao, Z. Jin, J. Ge, Z. Jiang, S. Chen, C. Liu and W. Xing, Identification of binuclear Co2N5 active sites for oxygen reduction reaction with more than one magnitude higher activity than single atom CoN4 site, *Nano Energy*, 2018, **46**, 396–403.

90 L. Zhou, P. Zhou, Y. Zhang, B. Liu, P. Gao and S. Guo, 3D star-like atypical hybrid MOF derived single-atom catalyst boosts oxygen reduction catalysis, *J. Energy Chem.*, 2021, **55**, 355–360.

91 R. Iqbal, S. Ali, G. Yasin, S. Ibraheem, M. Tabish, M. Hamza, H. Chen, H. Xu, J. Zeng and W. Zhao, A novel 2D $Co_3(HADQ)_2$ metal-organic framework as a highly active and stable electrocatalyst for acidic oxygen reduction, *Chem. Eng. J.*, 2022, **430**, 132642–132649.

92 J. Zhang, Z. Zhou, F. Wang, Y. Li and Y. Jing, Two-Dimensional Metal Hexahydroxybenzene Frameworks as Promising Electrocatalysts for an Oxygen Reduction Reaction, *ACS Sustainable Chem. Eng.*, 2020, **8**, 7472–7479.

93 R. Iqbal, M. Q. Sultan, S. Hussain, M. Hamza, A. Tariq, M. B. Akbar, Y. Ma and L. Zhi, The Different Roles of Cobalt and Manganese in Metal-Organic Frameworks for Supercapacitors, *Adv. Mater. Technol.*, 2021, **6**, 2000941–2000949.

94 D. Sheberla, L. Sun, M. A. Blood-Forsythe, S. Er, C. R. Wade, C. K. Brozek, A. Aspuru-Guzik and M. Dinca, High Electrical Conductivity in Ni-3(2,3,6,7,10,11-hexaiminotriphenylene) (2), a Semiconducting Metal-Organic Graphene Analogue, *J. Am. Chem. Soc.*, 2014, **136**, 8859–8862.

95 H. Wang, Y. Liang, Y. Li and H. Dai, Co(1-x)S-graphene hybrid: a high-performance metal chalcogenide electrocatalyst for oxygen reduction, *Angew. Chem., Int. Ed.*, 2011, **50**, 10969–10972.

96 T. Wang, C. Yang, Y. Liu, M. Yang, X. Li, Y. He, H. Li, H. Chen and Z. Lin, Dual-Shelled Multidoped Hollow Carbon Nanocages with Hierarchical Porosity for High-Performance Oxygen Reduction Reaction in Both Alkaline and Acidic Media, *Nano Lett.*, 2020, **20**, 5639–5645.

97 W. Zhang, P. Li, H. Zhao, L. Zong and L. Wang, Metal-free honeycomb-like electrocatalyst with high specific mass activity for accelerated oxygen reduction reaction in both alkaline and acidic media, *Appl. Surf. Sci.*, 2022, **579**, 152149–152156.

98 C. Yang, H. Jin, C. Cui, J. Li, J. Wang, K. Amine, J. Lu and S. Wang, Nitrogen and sulfur co-doped porous carbon sheets for energy storage and pH-universal oxygen reduction reaction, *Nano Energy*, 2018, **54**, 192–199.

99 K. Chen, K. Liu, P. An, H. Li, Y. Lin, J. Hu, C. Jia, J. Fu, H. Li, H. Liu, Z. Lin, W. Li, J. Li, Y.-R. Lu, T.-S. Chan, N. Zhang and M. Liu, Iron phthalocyanine with coordination induced electronic localization to boost oxygen reduction reaction, *Nat. Commun.*, 2020, **11**, 4173–4180.

100 R. Cao, R. Thapa, H. Kim, X. Xu, M. G. Kim, Q. Li, N. Park, M. Liu and J. Cho, Promotion of oxygen reduction by a bio-inspired tethered iron phthalocyanine carbon nanotube-based catalyst, *Nat. Commun.*, 2013, **4**, 2076–2082.

101 Y. Chen, R. Gao, S. Ji, H. Li, K. Tang, P. Jiang, H. Hu, Z. Zhang, H. Hao, Q. Qu, X. Liang, W. Chen, J. Dong, D. Wang and Y. Li, Atomic-Level Modulation of Electronic Density at Cobalt Single-Atom Sites Derived from Metal-Organic Frameworks: Enhanced Oxygen Reduction Performance, *Angew. Chem., Int. Ed.*, 2021, **60**, 3212–3221.

102 T. S. Olson, S. Pylypenko, J. E. Fulghum and P. Atanassov, Bifunctional Oxygen Reduction Reaction Mechanism on Non-Platinum Catalysts Derived from Pyrolyzed Porphyrins, *J. Electrochem. Soc.*, 2010, **157**, B54–B63.

103 J. Li, M. Chen, D. A. Cullen, S. Hwang, M. Wang, B. Li, K. Liu, S. Karakalos, M. Lucero, H. Zhang, C. Lei, H. Xu, G. E. Sterbinsky, Z. Feng, D. Su, K. L. More, G. Wang, Z. Wang and G. Wu, Atomically dispersed manganese catalysts for oxygen reduction in proton-exchange membrane fuel cells, *Nat. Catal.*, 2018, **1**, 935–945.

104 E. Luo, H. Zhang, X. Wang, L. Gao, L. Gong, T. Zhao, Z. Jin, J. Ge, Z. Jiang, C. Liu and W. Xing, Single-Atom Cr-N4 Sites Designed for Durable Oxygen Reduction Catalysis in Acid Media, *Angew. Chem., Int. Ed.*, 2019, **58**, 12469–12475.

105 F. Luo, A. Roy, L. Silvioli, D. A. Cullen, A. Zitolo, M. T. Sougrati, I. C. Oguz, T. Mineva, D. Teschner, S. Wagner, J. Wen, F. Dionigi, U. I. Kramm, J. Rossmeisl, F. Jaouen and P. Strasser, P-block single-metal-site tin/nitrogen-doped carbon fuel cell cathode catalyst for oxygen reduction reaction, *Nat. Mater.*, 2020, **19**, 1215–1223.

106 T. Y. Ma, J. Ran, S. Dai, M. Jaroniec and S. Z. Qiao, Phosphorus-Doped Graphitic Carbon Nitrides Grown In Situ on Carbon-Fiber Paper: Flexible and Reversible Oxygen Electrodes, *Angew. Chem., Int. Ed.*, 2015, **54**, 4646–4650.

107 K. Singh, F. Razmjooei and J.-S. Yu, Active sites and factors influencing them for efficient oxygen reduction reaction in metal-N coordinated pyrolyzed and non-pyrolyzed catalysts: a review, *J. Mater. Chem. A*, 2017, **5**, 20095–20119.

108 R. Hu, Y. Li, Q. Zeng and J. Shang, Role of active sites in N-coordinated Fe-Co dual-metal doped graphene for oxygen reduction and evolution reactions: A theoretical insight, *Appl. Surf. Sci.*, 2020, **525**, 146588–146596.

109 Z. Wang, X. Jin, C. Zhu, Y. Liu, H. Tan, R. Ku, Y. Zhang, L. Zhou, Z. Liu, S. J. Hwang and H. J. Fan, Atomically Dispersed Co2-N6 and Fe-N4 Costructures Boost Oxygen Reduction Reaction in Both Alkaline and Acidic Media, *Adv. Mater.*, 2021, **33**, e2104718.

110 S. H. Yin, J. Yang, Y. Han, G. Li, L. Y. Wan, Y. H. Chen, C. Chen, X. M. Qu, Y. X. Jiang and S. G. Sun, Construction of Highly Active Metal-Containing Nanoparticles and FeCo-N4

Composite Sites for the Acidic Oxygen Reduction Reaction, *Angew. Chem., Int. Ed.*, 2020, **59**, 21976–21979.

111 M. Jiang, F. Wang, F. Yang, H. He, J. Yang, W. Zhang, J. Luo, J. Zhang and C. Fu, Rationalization on high-loading iron and cobalt dual metal single atoms and mechanistic insight into the oxygen reduction reaction, *Nano Energy*, 2022, **93**, 106793–106802.

112 J. Wang, W. Liu, G. Luo, Z. Li, C. Zhao, H. Zhang, M. Zhu, Q. Xu, X. Wang, C. Zhao, Y. Qu, Z. Yang, T. Yao, Y. Li, Y. Lin, Y. Wu and Y. Li, Synergistic effect of well-defined dual sites boosting the oxygen reduction reaction, *Energy Environ. Sci.*, 2018, **11**, 3375–3379.

113 Y.-b. Chen, J.-j. Li, Y.-p. Zhu, J. Zou, H. Zhao, C. Chen, Q.-q. Cheng, B. Yang, L.-l. Zou, Z.-q. Zou and H. Yang, Vicinal Co atom-coordinated Fe–N–C catalysts to boost the oxygen reduction reaction, *J. Mater. Chem. A*, 2022, **10**, 9886–9891.

114 N. Yang, L. Peng, L. Li, J. Li, Q. Liao, M. Shao and Z. Wei, Theoretically probing the possible degradation mechanisms of an FeNC catalyst during the oxygen reduction reaction, *Chem. Sci.*, 2021, **12**, 12476–12484.

115 G. Yang, J. Zhu, P. Yuan, Y. Hu, G. Qu, B. A. Lu, X. Xue, H. Yin, W. Cheng, J. Cheng, W. Xu, J. Li, J. Hu, S. Mu and J. N. Zhang, Regulating Fe-spin state by atomically dispersed Mn-N in Fe-N-C catalysts with high oxygen reduction activity, *Nat. Commun.*, 2021, **12**, 1734.

116 H. Cai, G. Zhang, X. Zhang, B. Chen, Z. Lu, H. Xu, R. Gao and C. Shi, Engineering the Local Coordination Environment and Density of FeN4 Sites by Mn Cooperation for Electrocatalytic Oxygen Reduction, *Small*, 2022, **18**, e2200911.

117 T. He, Y. Chen, Q. Liu, B. Lu, X. Song, H. Liu, M. Liu, Y. N. Liu, Y. Zhang, X. Ouyang and S. Chen, Theory-Guided Regulation of FeN4 Spin State by Neighboring Cu Atoms for Enhanced Oxygen Reduction Electrocatalysis in Flexible Metal-Air Batteries, *Angew. Chem., Int. Ed.*, 2022, e202201007, DOI: **10.1002/anie.202201007**.

118 C. Du, Y. Gao, H. Chen, P. Li, S. Zhu, J. Wang, Q. He and W. Chen, A Cu and Fe dual-atom nanozyme mimicking cytochrome c oxidase to boost the oxygen reduction reaction, *J. Mater. Chem. A*, 2020, **8**, 16994–17001.

119 S. Song, X. M. Zhang, X. L. Xu, C. C. Wu, H. Q. Li, Z. X. Xia, S. S. Yu, S. L. Wang and G. Q. Sun, Iron, Copper and Nitrogen Co-doped Carbon with Enhanced Electrocatalytic Activity towards Oxygen Reduction, *ChemElectroChem*, 2020, **7**, 3116–3122.

120 H. Li, S. Di, P. Niu, S. Wang, J. Wang and L. Li, A durable half-metallic diatomic catalyst for efficient oxygen reduction, *Energy Environ. Sci.*, 2022, **15**, 1601–1610.

121 Z. Li, H. He, H. Cao, S. Sun, W. Diao, D. Gao, P. Lu, S. Zhang, Z. Guo, M. Li, R. Liu, D. Ren, C. Liu, Y. Zhang, Z. Yang, J. Jiang and G. Zhang, Atomic Co/Ni dual sites and Co/Ni alloy nanoparticles in N-doped porous Janus-like carbon frameworks for bifunctional oxygen electrocatalysis, *Appl. Catal., B*, 2019, **240**, 112–121.

122 Q. Zhang, P. Kumar, X. Zhu, R. Daiyan, N. M. Bedford, K. H. Wu, Z. Han, T. Zhang, R. Amal and X. Lu, Electronically Modified Atomic Sites Within a Multicomponent Co/Cu Composite for Efficient Oxygen Electroreduction, *Adv. Energy Mater.*, 2021, **11**, 2100303–2100313.

123 S. S. A. Shah, T. Najam, M. S. Javed, M. M. Rahman and P. Tsiakaras, Novel Mn-/Co-Nx Moieties Captured in N-Doped Carbon Nanotubes for Enhanced Oxygen Reduction Activity and Stability in Acidic and Alkaline Media, *ACS Appl. Mater. Interfaces*, 2021, **13**, 23191–23200.

124 J. Wang, R. Xu, Y. Sun, Q. Liu, M. Xia, Y. Li, F. Gao, Y. Zhao and J. S. Tse, Identifying the Zn–Co binary as a robust bifunctional electrocatalyst in oxygen reduction and evolution reactions via shifting the apexes of the volcano plot, *J. Energy Chem.*, 2021, **55**, 162–168.

125 L. Cao, Y. Shao, H. Pan and Z. Lu, Designing Efficient Dual-Metal Single-Atom Electrocatalyst TMZnN6 (TM = Mn, Fe, Co, Ni, Cu, Zn) for Oxygen Reduction Reaction, *J. Phys. Chem. C*, 2020, **124**, 11301–11307.

126 J. Li, S. Chen, N. Yang, M. Deng, S. Ibraheem, J. Deng, J. Li, L. Li and Z. Wei, Ultrahigh-Loading Zinc Single-Atom Catalyst for Highly Efficient Oxygen Reduction in Both Acidic and Alkaline Media, *Angew. Chem., Int. Ed.*, 2019, **58**, 7035–7039.

127 J. Mueller-Huelstede, D. Schonvogel, H. Schmies, P. Wagner, A. Dyck and M. Wark, Incorporation of Activated Biomasses in Fe-N-C Catalysts for Oxygen Reduction Reaction with Enhanced Stability in Acidic Media, *ACS Appl. Energy Mater.*, 2021, **4**, 6912–6922.

128 D. Xia, X. Yang, L. Xie, Y. Wei, W. Jiang, M. Dou, X. Li, J. Li, L. Gan and F. Kang, Direct Growth of Carbon Nanotubes Doped with Single Atomic Fe–N_4 Active Sites and Neighboring Graphitic Nitrogen for Efficient and Stable Oxygen Reduction Electrocatalysis, *Adv. Funct. Mater.*, 2019, **29**, 1906174–1906183.

129 X. Wan, X. Liu, Y. Li, R. Yu, L. Zheng, W. Yan, H. Wang, M. Xu and J. Shui, Fe–N–C electrocatalyst with dense active sites and efficient mass transport for high-performance proton exchange membrane fuel cells, *Nat. Catal.*, 2019, **2**, 259–268.

130 Q. Wang, Y. Yang, F. Sun, G. Chen, J. Wang, L. Peng, W. T. Chen, L. Shang, J. Zhao, D. Sun-Waterhouse, T. Zhang and G. I. N. Waterhouse, Molten NaCl-Assisted Synthesis of Porous Fe-N-C Electrocatalysts with a High Density of Catalytically Accessible FeN_4 Active Sites and Outstanding Oxygen Reduction Reaction Performance, *Adv. Energy Mater.*, 2021, **11**, 2100219–2100227.

131 L. Jiao, J. Li, L. L. Richard, Q. Sun, T. Stracensky, E. Liu, M. T. Sougrati, Z. Zhao, F. Yang, S. Zhong, H. Xu, S. Mukerjee, Y. Huang, D. A. Cullen, J. H. Park, M. Ferrandon, D. J. Myers, F. Jaouen and Q. Jia, Chemical vapour deposition of Fe–N–C oxygen reduction catalysts with full utilization of dense Fe–N4 sites, *Nat. Mater.*, 2021, **20**, 1385–1391.